RSC Advances

PAPER

Published on 13 July 2026
Licensed under CC-BY-NC 4.0

Check for updates

Cite this: DOI: 10.1039/d6ra03112a

WSi_2N_4/XSe and $WSiGeN_4$/XSe (X=Al, Ga, and In) heterostructures for photocatalytic water splitting: a DFT investigation

Emircan Turgut,[a] Sefer Bora Lisesivdin,[b] Aysenur Gencer,[c] Ozge Surucu,[d] Gozde Altuntas,[e] Bulent Bostan,[e] Fatih Himmet [a] and Gokhan Surucu *[f]

The research for an effective photocatalyst is ongoing, and this study considers the WSi_2N_4/XSe and $WSiGeN_4$/XSe (X = Al, Ga, and In) heterostructures for photocatalytic water splitting using Density Functional Theory. The heterostructures are constructed using a 7 × 7 × 1 supercell for the WSi_2N_4 and $WSiGeN_4$ monolayers and 2 × 2 × 1 supercell for the XSe monolayers. The structural optimizations reveal that the heterostructures with the InSe monolayers have positive binding energy, which reveals their structural instability. The WSi_2N_4/XSe and $WSiGeN_4$/XSe (X = Al and Ga) heterostructures have been further considered for their mechanical and thermodynamic stabilities, where all the heterostructures are structurally, mechanically, and thermodynamically stable. The electronic properties of WSi_2N_4/XSe and $WSiGeN_4$/XSe (X = Al and Ga) heterostructures are studied in detail using PBE and HSE methods. The WSi_2N_4/AlSe, WSi_2N_4/GaSe, and $WSiGeN_4$/AlSe heterostructures have band gaps as 1.83 eV, 1.66 eV and 1.69 eV, respectively, that satisfy the band gap requirement for photocatalytic water splitting. In addition, the valence band and conduction band levels are determined that must satisfy the redox potential. This analysis reveals that the WSi_2N_4/AlSe and WSi_2N_4/GaSe heterostructures have an S-scheme mechanism, while the $WSiGeN_4$/AlSe heterostructure has a type-II mechanism. Furthermore, the optical properties and solvent effect are investigated to reveal the performance of these heterostructures further. The present study determines the stability of WSi_2N_4/XSe and $WSiGeN_4$/XSe heterostructures and examines their photocatalytic water splitting potential in detail. It is therefore posited that the results presented in this study will serve as a guide to inform future studies and pave the way for new research in this field.

Received 13th April 2026
Accepted 28th June 2026

DOI: 10.1039/d6ra03112a

rsc.li/rsc-advances

1. Introduction

The energy requirement is increasing due to population growth, industrial development, and new technologies. This trend poses significant challenges for sustainable energy management and necessitates innovative solutions to meet future demands. Innovative energy management techniques, including the integration of renewable sources and advanced technologies, are essential to address the growing energy demands and ensure sustainability. To achieve this, renewable energy sources are crucial for fostering a sustainable energy future, as they provide cleaner alternatives that can significantly reduce carbon emissions and enhance energy security.[1] This approach not only mitigates environmental impacts but also aligns with global efforts to combat climate change and promotes long-term energy sustainability by facilitating the transition away from fossil fuels towards more resilient energy systems that leverage diverse renewable resources.[2,3] Hydrogen energy is a promising solution among these renewable energy sources as it offers a clean and versatile energy carrier that can support various applications, including transportation and power generation.[4] By harnessing hydrogen produced from renewable sources, energy security could be enhanced, and greenhouse gas emissions could be reduced while addressing the challenges posed by climate change.[5] For a hydrogen economy, hydrogen production is essential to ensure a reliable supply of this clean energy carrier. The photocatalytic water splitting is one of the hydrogen production methods that has gained significant attention due to its potential for sustainable hydrogen generation using solar energy.[6] This method utilizes photocatalysts to efficiently convert water into hydrogen and oxygen, aligning with global sustainability goals.[7]

The search for an effective photocatalyst is ongoing that can meet the stringent requirements for efficiency, stability, and

[a]Graduate School of Natural and Applied Sciences, Gazi University, Ankara, 06500, Türkiye
[b]Department of Physics, Faculty of Science, Gazi University, Ankara 06500, Türkiye
[c]Department of Physics, K. O. Faculty of Science, Karamanoglu Mehmetbey University, Karaman 70200, Türkiye
[d]Department of Energy Systems Engineering, Faculty of Engineering and Natural Sciences, Ankara Yildirim Beyazit University, Ankara, 06010, Türkiye
[e]Department of Metallurgical and Materials Engineering, Faculty of Technology, Gazi University, Ankara 06500, Türkiye
[f]Department of Energy Systems Engineering, Faculty of Technology, Gazi University, Ankara 06500, Türkiye. E-mail: gokhansurucu@gazi.edu.tr

© 2026 The Author(s). Published by the Royal Society of Chemistry

cost-effectiveness in hydrogen production.[8] The 2D materials, after realizing the discovery of graphene, are promising for enhancing photocatalytic performance due to their unique properties, including high surface area and excellent electron mobility.[9] As research progresses, these materials may play a pivotal role in advancing sustainable hydrogen production technologies. The integration of advanced 2D materials, such as graphitic carbon nitride, into photocatalytic systems could significantly enhance the efficiency and effectiveness of hydrogen production methods.[10] In addition, there are several studies that investigate the heterostructures of 2D materials.[11–13] These studies highlight the potential of combining different 2D materials to create efficient photocatalysts, further advancing the field of sustainable hydrogen production through innovative material design.[11–13] The ongoing exploration of 2D material heterostructures is vital for developing advanced photocatalysts that can meet the increasing global energy demands while promoting sustainable hydrogen production.

Recently, WSi_2N_4 has been synthesized experimentally[14] and a new 2D material family called MA_2Z_4 is introduced.[15,16] This development opens new avenues for research into the photocatalytic applications of MA_2Z_4 materials, potentially enhancing hydrogen production efficiency and sustainability.[17–19] Furthermore, the Janus structures of MA_2Z_4 materials are investigated, where they are essential for achieving improved photocatalytic performance by enabling unique surface properties and charge separation mechanisms.[20–23] To get a heterostructure with this material family is ongoing research.[24] Li *et al.*[25] have been investigated AlO/WSi_2N_4 van der Waals heterostructure, and they have found that this heterostructure has type-II band alignment, enabling the water splitting under light irradiation. In another study, the GaSe/WSi_2N_4 heterostructure is considered for the photocatalytic hydrogen generation, and it has been found that this heterostructure has an S-scheme band alignment with a 2.02 eV band gap.[26] The WSi_2N_4/$MoSi_2N_4$ heterostructure has also been studied, which has a type-II band alignment with a 2.007 eV band gap.[27] In this study, the WSi_2N_4 and $WSiGeN_4$ monolayers are chosen. Furthermore, the AlSe, GaSe, and InSe monolayers are chosen as potential candidates to form a heterostructure with these monolayers. The development of 2D heterostructures represents a promising avenue for enhancing photocatalytic activity, potentially transforming hydrogen production and contributing significantly to sustainable energy solutions. In this study, the WSi_2N_4/XSe and $WSiGeN_4$/XSe (X = Al, Ga, and In) heterostructures are investigated to reveal their potential for photocatalytic water splitting. The findings from this investigation may provide valuable insights into the design and optimization of advanced photocatalysts for efficient hydrogen production. The results of this study could pave the way for innovative photocatalytic systems that leverage the unique properties of these 2D heterostructures, enhancing overall hydrogen production efficiency.

2. Calculation details

This study presents the hydrogen production performance of WSi_2N_4/XSe and $WSiGeN_4$/XSe heterostructures investigated using the Vienna *Ab initio* Simulation Package (VASP).[28,29] VASP is based on Density Functional Theory (DFT) and the exchange and correlation terms for the electron–electron interactions are considered using the Perdew–Burke–Ernzerhof (PBE) functional[30] within the Generalized Gradient Approximation (GGA) during the calculations. Meanwhile, the interactions between the electrons and the ions are performed using the Projector Augmented Wave (PAW) method.[31,32] The heterostructures are obtained using the individual monolayers of the WSi_2N_4, $WSiGeN_4$, and XSe. An energy cut-off is taken as 530 eV, 530 eV, 320 eV, 285 eV and 285 eV for the WSi_2N_4, $WSiGeN_4$, AlSe, GaSe, and InSe monolayers, respectively. The gamma-centered[33] *k*-points are taken as $5 \times 5 \times 1$ for all the monolayers. The energy cut-off is taken as 500 eV for the heterostructures along with the $5 \times 5 \times 1$ Monkhorst–Pack *k*-points.[34] The W, Si, Ge, N, Al, Ga, and Se atoms are provided with the valence electron distributions as $5d^4 6s^2$, $3s^2 3p^2$, $4s^2 4p^2$, $2s^2 2p^3$, $3s^2 3p^1$, $4s^2 4p^1$, and $4s^2 4p^4$, respectively. The optimizations are carried out until the convergence criteria are reached as 10^{-6} eV and 10^{-3} eV Å^{-1} for energy and force, respectively. The interactions between the layers should be prevented; thus, 15 Å vacuum space is included for these heterostructures. Furthermore, the DFT-D3 correction is included for the van der Waals correction.[35] The optimized heterostructures are further considered for mechanical stability. For this purpose, the ELASTOOL package[36,37] is used to obtain the elastic constants, which are employed for the determination of the mechanical stability. For a good photocatalyst, it is essential to have a suitable band gap to generate the electron and hole pairs. Therefore, the electronic band structures are obtained using the PBE method as well as the Heyd–Scuseria–Ernzerhof (HSE) hybrid functional.[38] 0.2 Å^{-1} screening parameter is employed, and the exchange part is mixed with 25% of the exact non-local Hartree–Fock exchange[39] for the HSE method. In addition, the band structures are visualized using the Sumo tools.[40] The execution of the Bader partial charge calculations has been facilitated through the utilization of the VASP, while the subsequent analysis has been conducted employing an algorithm that has been developed by the Henkelman group,[41] which is grounded in Bader's original proposal.[42] The thermodynamic stabilities of the investigated heterostructures are verified at elevated temperatures using *ab initio* molecular dynamics (AIMD) simulations accelerated by VASP's automated on-the-fly Machine Learning Force Field (MLFF) feature.[43,44] All MD calculations are carried out within the canonical ensemble (N V T) using a Langevin thermostat (MDALGO = 3) and a standard integration time step of 1.0 fs (POTIM = 1.0). To construct a highly reliable potential energy surface (PES), a rigorous two-stage machine learning workflow is employed. In the first stage, an exploratory 2.0 ps (2000 steps) training run is conducted to heat the structure from 100 K to 300 K (ML_MODE = train, ML_ISTART = 0). During this initial heating phase, a strict Bayesian force error threshold of 0.002 eV Å^{-1} (ML_CTIFOR = 0.002) is applied to trigger intensive *ab initio* DFT updates, capturing a diverse array of foundational atomic environments. In the second stage, the pre-trained database is loaded (ML_ISTART = 1) to execute an extensive 10.0 ps (10 000 steps) production and thermal stability

© 2026 The Author(s). Published by the Royal Society of Chemistry

verification trajectory centered around room temperature (300–350 K). Within this production phase, the Bayesian force threshold is updated to 0.02 eV Å^{-1} (ML_CTIFOR = 0.02), allowing the MLFF to handle the majority of the integration steps while seamlessly querying the first-principles electronic structure back-end (EDIFF = 10^{-6} eV) only when unmapped, high-error structural configurations were encountered. The descriptors based on the Gaussian representation of the atomic distributions[44,45] are used for the MLFF generated potential energy surface. The Bayesian linear regression[43,46] is employed in order to obtain the energy, force, and stress components. The VESTA software[47] is used for the crystal structure visualization. In order to ascertain the solvent effects in these heterostructures, the present study employs the VASPSOL software package,[48,49] in which the dielectric constant of the water solvent employed as 78.4.

3. Results and discussions

3.1 Structural and stability considerations for the WSi_2N_4/XSe and $WSiGeN_4$/XSe (X = Al, Ga, and In) heterostructures

In order to obtain the WSi_2N_4/XSe and $WSiGeN_4$/XSe (X = Al, Ga, and In) heterostructures, the individual monolayers are first optimized. The WSi_2N_4 and $WSiGeN_4$ monolayers have been studied previously in 50 by our group. The XSe (X = Al and Ga) monolayers are optimized for this study. Table 1 lists the optimized lattice parameters for these monolayers, which have a hexagonal lattice. The optimized lattice parameters are well consistent with the available literature. In order to have a well-matched heterostructure, the lattice parameters should be very close to the lattice parameters of each monolayer. For this purpose, the supercells are taken as 7 × 7 × 1 supercell for the WSi_2N_4 and $WSiGeN_4$ monolayers and 2 × 2 × 1 supercell for XSe monolayers. Table 1 also lists the lattice parameters for the supercells, where the consistency between the lattice parameters of each monolayer can be seen.

Fig. 1 shows the five different stackings that are obtained using the 7 × 7 × 1 supercell for the WSi_2N_4 and $WSiGeN_4$ monolayers and 2 × 2 × 1 supercell for XSe monolayers, where their crystal structures are given in Fig. S1 in the SI File. These heterostructures are optimized, and the binding energies of these monolayers are calculated using eqn (1), where $E_{WSi_2N_4/XSe}$, $E_{WSi_2N_4}$, and E_{XSe} correspond to the total energy of the heterostructure, 7 × 7 × 1 supercell of the WSi_2N_4 monolayer, and 2 × 2 × 1 supercell of the XSe monolayer, respectively. In eqn (1), the total energy of the WSi_2N_4 monolayer should be considered as the total energy of 7 × 7 × 1 supercell of the $WSiGeN_4$ monolayer in the corresponding heterostructures. Table 2 lists the binding energy values for each stacking for WSi_2N_4/XSe and $WSiGeN_4$/XSe heterostructures, respectively. If the heterostructure has a negative binding energy value, this indicates the thermodynamic stability of that structure. According to Table 2, the lowest binding energy for the WSi_2N_4/XSe and $WSiGeN_4$/XSe heterostructures belongs to A1 stacking, except those composed of the InSe monolayers. The positive binding energy for the WSi_2N_4/InSe and $WSiGeN_4$/InSe heterostructures may be due to lattice mismatch between monolayers, where InSe monolayer has a higher lattice constant compared to the other monolayers. The lattice mismatch values are obtained as 0.08%, 1.60%, 8.47%, 2.23%, 0.57%, and 6.46% for the WSi_2N_4/AlSe, WSi_2N_4/GaSe, WSi_2N_4/InSe, $WSiGeN_4$/AlSe, $WSiGeN_4$/GaSe, and $WSiGeN_4$/InSe, respectively. In order to ensure the efficacy of a heterostructure, it is essential to maintain a lattice mismatch of less than 5% between the two layers.[56–58] This principle is supported by numerical calculations which indicate a mismatch of below 5% except for the WSi_2N_4/InSe and $WSiGeN_4$/InSe, thereby validating the structural stability of the heterostructures. The observed lattice mismatch for the WSi_2N_4/AlSe, WSi_2N_4/GaSe, $WSiGeN_4$/AlSe, and $WSiGeN_4$/GaSe heterostructures is within 5% of the acceptable range of lattice mismatch, as reported in the existing literature.[56–58] It is worth noting that while lattice matching can occasionally be modulated by constructing large, high-index supercell expansions or by applying external biaxial strain fields, such structural modifications were not extended to the InSe-bearing heterostructures. Forcing the large natural lattice mismatches of WSi_2N_4/InSe (8.47%) and WSiGeN4/InSe (6.46%) down to compliant levels below the 5\% stability ceiling would require inducing high, non-physical elastic strains. Such severe strain states would compromise the integrity of the standalone layers and mask the authentic, freestanding electronic properties of the materials. Furthermore, the calculated positive binding energies for these configurations serve as a definitive thermodynamic bottleneck, demonstrating that the chemical affinity at the interface is fundamentally unfavorable. Consequently, regardless of the stacking configuration or supercell arrangement employed, the InSe-based structures remain inherently unstable and prone to phase separation, justifying their exclusion from subsequent optoelectronic and catalytic evaluations. To date, the GaSe/WSi_2N_4 heterostructure[26] remains the sole subject of study in the existing literature. This study[26] has demonstrated that model A exhibits a negative binding energy. Therefore, the outcomes derived from this study are in accordance with the findings of the aforementioned work.[26] In the subsequent section, the A1 configuration will be utilized for

Table 1 Lattice parameters for WSi_2N_4, $WSiGeN_4$, and XSe (X = Al, Ga, and In) monolayers and lattice parameters for 7 × 7 × 1 supercell for the WSi_2N_4 and $WSiGeN_4$ monolayers and 2 × 2 × 1 supercell for XSe monolayers

Monolayer	a (Å) for unit cell	a (Å) for supercell
WSi_2N_4	2.94 (ref. 50) 2.91 (ref. 51)	7.77
$WSiGeN_4$	3.00 (ref. 50) 2.97 (ref. 52)	7.94
AlSe	3.88 3.776 (ref. 53)	7.76
GaSe	3.95 3.81 (ref. 54)	7.90
InSe	4.24 3.94 (ref. 55)	8.49

© 2026 The Author(s). Published by the Royal Society of Chemistry

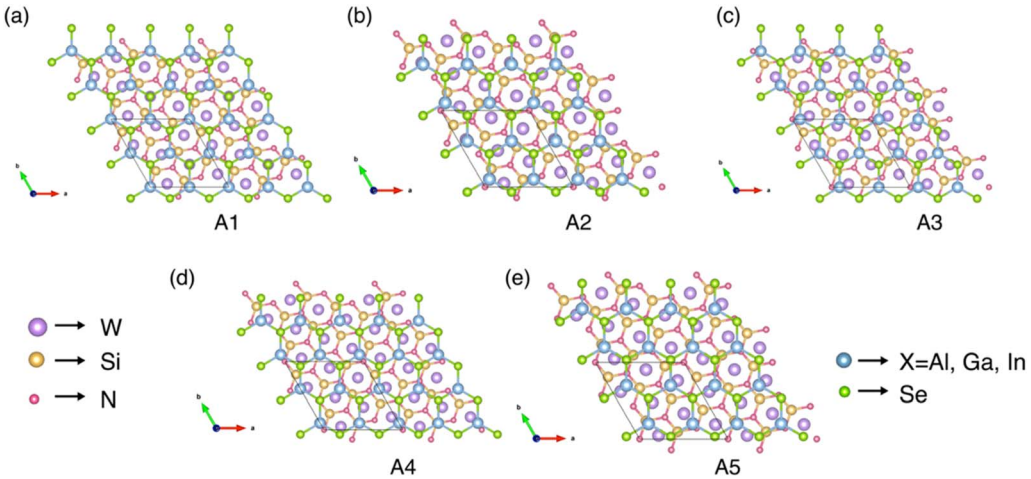


Fig. 1 Crystal structures for (a) A1, (b) A2, (c) A3, (d) A4, and (e) A5 stackings that are obtained using supercells of WSi_2N_4, $WSiGeN_4$ and XSe (X = Al, Ga, and In) heterostructures monolayers.

Table 2 Binding energies (E_b) for WSi_2N_4/XSe and $WSiGeN_4$/XSe (X = Al, Ga, and In) heterostructures

Heterostructure		E_b (eV)	Heterostructure		E_b (eV)
WSi_2N_4/AlSe	A1	−0.15	$WSiGeN_4$/AlSe	A1	−0.25
	A2	0.70		A2	1.34
	A3	0.70		A3	1.38
	A4	−0.09		A4	−0.19
	A5	0.70		A5	1.37
WSi_2N_4/GaSe	A1	−0.19	$WSiGeN_4$/GaSe	A1	−0.41
	A2	−0.10		A2	1.30
	A3	−0.03		A3	1.29
	A4	−0.07		A4	0.13
	A5	0.01		A5	1.29
WSi_2N_4/InSe	A1	0.98	$WSiGeN_4$/InSe	A1	0.53
	A2	0.98		A2	0.52
	A3	0.98		A3	0.25
	A4	0.98		A4	0.37
	A5	0.98		A5	0.53

further analysis based on its proven structural stability for the WSi_2N_4/XSe and WSiGeN4/XSe (X = Al and Ga) heterostructures.

$$E_b = E_{WSi_2N_4/XSe} - E_{WSi_2N_4} - E_{XSe} \quad (1)$$

The A1 stacking of the WSi_2N_4/XSe and $WSiGeN_4$/XSe (X = Al and Ga) heterostructures are further examined to reveal their mechanical and thermodynamical stabilities. For the mechanical stability, the elastic constants are calculated and listed in Table 3 for these heterostructures. These heterostructures have a hexagonal crystal structure, and they possess the required elastic constants, C_{11} and C_{12}, which are characteristic of this symmetry. According to Table 3, these heterostructures have C_{11} >0 and $C_{11} > |C_{12}|$ which are Born stability criteria for the hexagonal crystal symmetry.[59,60] Therefore, these heterostructures satisfy the Born stability criteria, which indicates their mechanical stability. Table 3 also lists the Young's modulus, shear modulus, and Poisson's ratio for these heterostructures. The Young's modulus is a measure of the stiffness of a material and according to the table, the heterostructures with AlSe monolayers are stiffer than the others. The shear modulus is a measure of the material's deformations under shear stress. The heterostructures have similar behavior according to Young's modulus. The Poisson's ratio is the contraction or expansion in perpendicular directions when stretched or compressed. These heterostructures have a similar Poisson's ratio according to Table 3.

The thermodynamic stabilities of these heterostructures are examined with the *ab initio* molecular dynamics (AIMD) simulations using VASP. The AIMD simulations demand computational resources, so the machine learning force field (MLFF) implemented in VASP is employed in order to accelerate these simulations. Fig. 2 shows the total energy change as a function of time during the AIMD simulations for the WSi_2N_4/XSe and $WSiGeN_4$/XSe (X = Al and Ga) heterostructures. The temperature change as a function of time during the AIMD simulations is shown in Fig. 3 for these heterostructures. As illustrated in these figures, the fluctuations in both energy and temperature are small for all heterostructures, which indicates the thermodynamic stability of these heterostructures at 300 K. In addition, the crystal structures are shown in the figures at the beginning and end of the simulations, where the structures are almost unchanged. For the reliability of these calculations, Bayesian error of the MLFF and root mean square error of forces

Table 3 Elastic constants (C_{11} and C_{12} in N m^{-1}), Young's modulus (Y_{2D} in N m^{-1}), shear modulus (G_{2D} in N m^{-1}), and Poisson's ratio (ν) of the WSi_2N_4/XSe and $WSiGeN_4$/XSe (X = Al and Ga) heterostructures

Heterostructure	C_{11}	C_{12}	Y_{2D}	G_{2D}	ν
WSi_2N_4/AlSe	619.23	162.46	576.61	228.39	0.26
WSi_2N_4/GaSe	609.80	159.61	568.02	225.09	0.26
$WSiGeN_4$/AlSe	553.76	154.06	510.90	199.85	0.28
$WSiGeN_4$/GaSe	544.80	149.70	503.66	197.55	0.27

© 2026 The Author(s). Published by the Royal Society of Chemistry

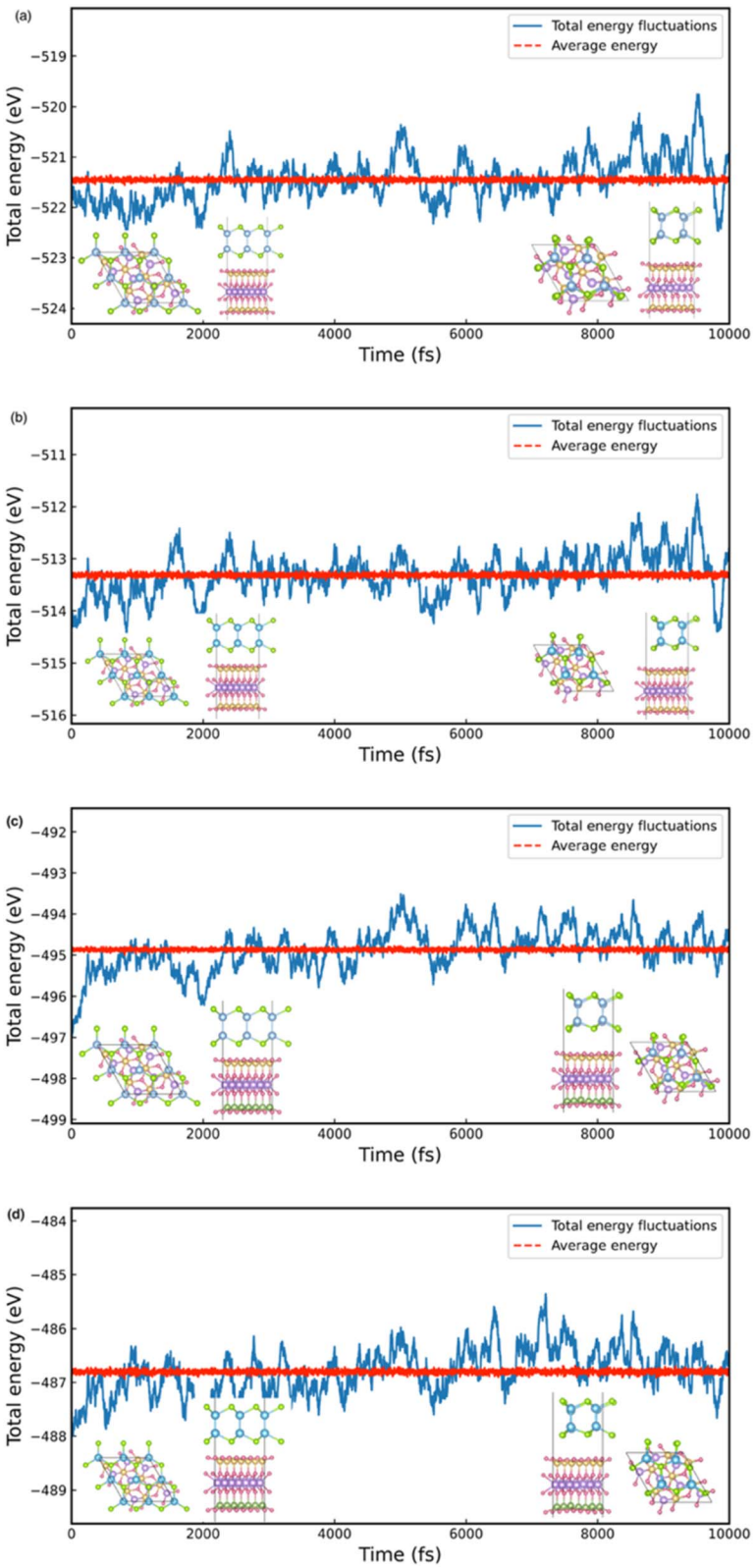


Fig. 2 The total energy change during a 10 000 fs time interval for the (a) WSi_2N_4/AlSe, (b) WSi_2N_4/GaSe, (c) $WSiGeN_4$/AlSe, and (d) $WSiGeN_4$/GaSe heterostructures during AIMD simulations.

are calculated and given in Fig. S2, S3, S4, and S5, for WSi_2N_4/AlSe, WSi_2N_4/GaSe, $WSiGeN_4$/AlSe, and $WSiGeN_4$/GaSe heterostructures, respectively. As quantified in Fig. S2–S5, throughout the entire 10 ps production trajectory the instantaneous Bayesian force error remained below the ML_CTIFOR threshold of 0.02 eV $Å^{-1}$ for the great majority of the MD steps, with only

© 2026 The Author(s). Published by the Royal Society of Chemistry

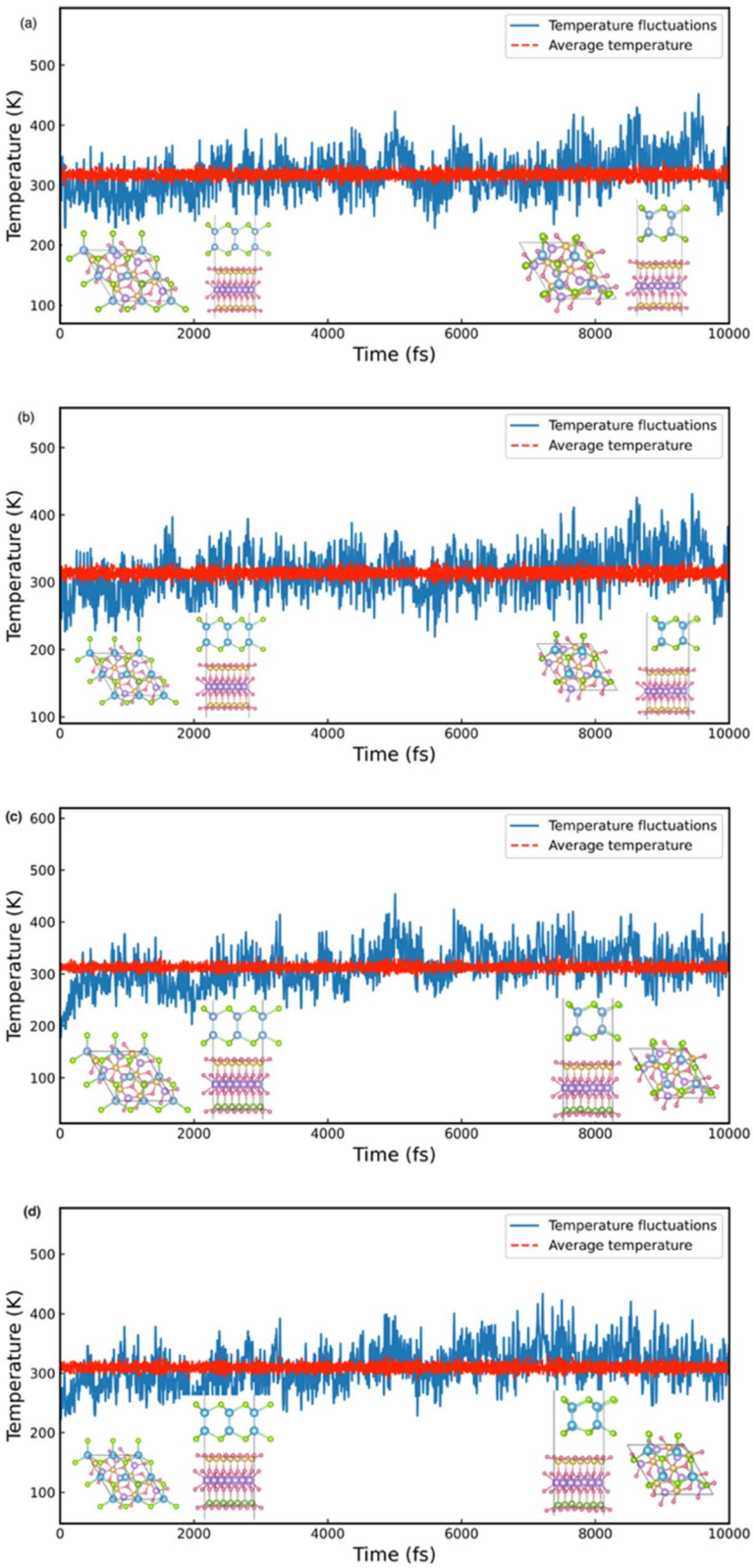


Fig. 3 The temperature change during a 10 000 fs time interval for the (a) WSi_2N_4/AlSe, (b) WSi_2N_4/GaSe, (c) $WSiGeN_4$/AlSe, and (d) $WSiGeN_4$/GaSe heterostructures during AIMD simulations.

sparse on-the-fly DFT updates triggered to repair the model. The root-mean-square error of the predicted forces relative to the reference DFT calculations stayed well below this threshold, confirming the fidelity of the MLFF potential energy surface against the underlying *ab initio* landscape and validating the use of accelerated dynamics for assessing room-temperature

© 2026 The Author(s). Published by the Royal Society of Chemistry

structural stability. Therefore, these heterostructures are promising candidates for the photocatalytic water splitting due to having negative binding energy, elastic constants satisfying mechanical stability criteria, small total energy and temperature fluctuations without changing crystal structure. As a result, their potential for photocatalytic water splitting is further examined.

3.2 Electronic properties for the WSi_2N_4/XSe and $WSiGeN_4$/XSe (X = Al and Ga) heterostructures

After these structural and stability considerations, the electronic properties are investigated in detail. For this purpose, the electronic band structures are determined using the GGA-PBE method for these heterostructures. The GGA-PBE method is widely employed in the literature, and it is also well-known that this method underestimates the band gaps compared to the experimental values. Therefore, the HSE method is employed in order to obtain the band gaps closer to the experimental results. In the previous study, the band gap of $WSiGeN_4$ monolayer was found to be as 1.59 eV obtained using the GGA-PBE method, while it was found to be as 2.12 eV band gap obtained using the HSE method, respectively.[50] The AlSe, and GaSe monolayers have band gaps of 1.87 and 1.22 eV, respectively, that are obtained using the GGA-PBE method, as shown in Fig. S6 in the SI File. Fig. S7 shows the band gaps obtained using the HSE method for the AlSe and GaSe monolayers, where they are 2.56 eV and 2.20 eV, respectively. These band gap values show that they are suitable for constructing heterostructures. The electronic band structures for the WSi_2N_4/XSe and $WSiGeN_4$/XSe heterostructures are obtained using both the GGA-PBE and the HSE methods. Fig. S8 shows the electronic band structures obtained using the GGA-PBE method for the WSi_2N_4/XSe and $WSiGeN_4$/XSe heterostructures, and Fig. 4 shows the electronic band structures obtained using the HSE method for these heterostructures. According to Fig. S8, the WSi_2N_4/AlSe and WSi_2N_4/GaSe heterostructures have direct band gaps with 1.32 eV and 0.95 eV, respectively, whereas the $WSiGeN_4$/AlSe and $WSiGeN_4$/GaSe heterostructures have indirect band gaps

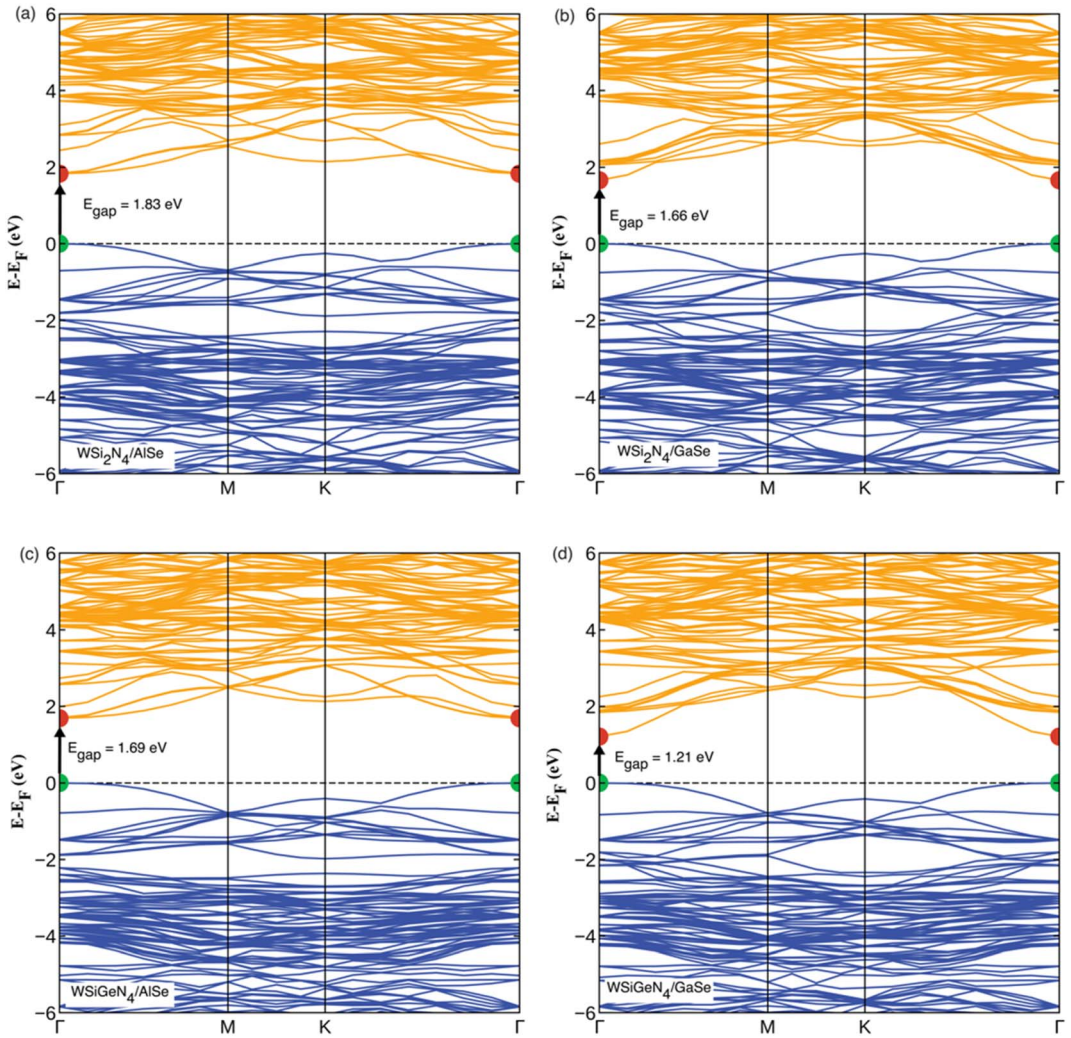


Fig. 4 Electronic band structures obtained using the HSE method for (a) WSi_2N_4/AlSe, (b) WSi_2N_4/GaSe, (c) $WSiGeN_4$/AlSe, and (d) $WSiGeN_4$/GaSe heterostructures.

© 2026 The Author(s). Published by the Royal Society of Chemistry

with 1.24 eV and 0.60 eV, respectively. These band gap values are low according to the required band gap for the photocatalytic water splitting. However, as is well known, the GGA-PBE method underestimates the band gap values for semiconductors. So, the results from the HSE method must be considered for a reliable discussion. As illustrated in Fig. 4, the direct band gaps are 1.83 eV, 1.66 eV, 1.69 eV, and 1.21 eV for the WSi_2N_4/AlSe, WSi_2N_4/GaSe, $WSiGeN_4$/AlSe, and $WSiGeN_4$/GaSe heterostructures, respectively. The research undertaken in the literature has found the band gap of the GaSe/WSi_2N_4 heterostructure to be 2.02 eV.[26] The findings of this study demonstrate the existence of a discrepancy in this study[26] which can be attributed to the inherent differences between the heterostructures. The HSE method results indicate that the $WSiGeN_4$/GaSe heterostructure is the only structure that does not satisfy the band gap requirement for photocatalytic water splitting. Meanwhile, the band gap requirement is satisfied by the heterostructure of WSi_2N_4/AlSe, WSi_2N_4/GaSe, and $WSiGeN_4$/AlSe, which has a band gap value greater than 1.23 eV. Consequently, these heterostructures are promising candidates for effective photocatalysis, as they meet the necessary band gap requirements.

3.3 Work function studies for the WSi_2N_4/XSe (X = Al and Ga) and $WSiGeN_4$/AlSe heterostructures

As a critical component of the analysis of interface characteristics and band alignment in heterojunctions, the work function plays a pivotal role. Eqn (2) provides a method for its calculation.[62]

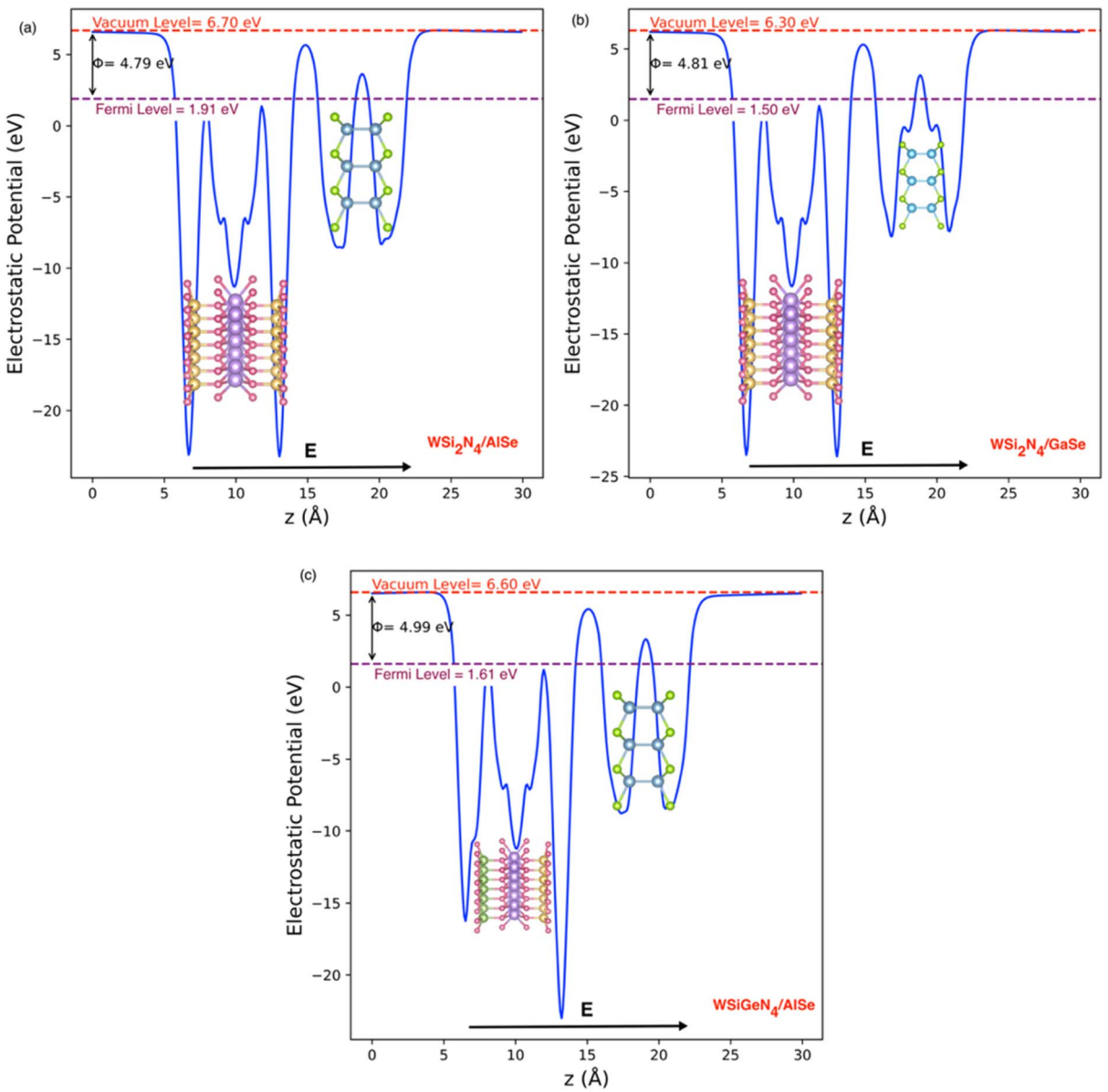


Fig. 5 Electrostatic potential across the *z*-direction for (a) WSi_2N_4/AlSe, (b) WSi_2N_4/GaSe, and (c) $WSiGeN_4$/AlSe heterostructures.

© 2026 The Author(s). Published by the Royal Society of Chemistry

$$W = E_{vac} - E_F \quad (2)$$

In this equation, W, E_{vac}, and E_F correspond to the work function, vacuum energy level, and Fermi level, respectively. The following fundamental property is represented by the minimum amount of energy required to cause an electron to become free and move away from the surface of a particular material. Fig. 5 shows the electrostatic potential across the z-direction for these heterostructures. As evident from the figure, the work functions are 4.79 eV, 4.81 eV, and 4.99 eV for the WSi_2N_4/AlSe, WSi_2N_4/GaSe, and $WSiGeN_4$/AlSe heterostructures, respectively. The work function difference between the monolayers results in a built-in electric field in these heterostructures, as shown as a black arrow in the figures, which is directed from WSi_2N_4 and $WSiGeN_4$ to AlSe and GaSe monolayers. Furthermore, the $WSiGeN_4$ monolayer has an asymmetric potential profile due to its Janus structure.

3.4 Absolute band-edge alignment and pH-dependent straddling for the WSi_2N_4/XSe (X = Al and Ga) and $WSiGeN_4$/AlSe heterostructures

The absolute band-edge positions on the vacuum scale (E_{vacuum} = 0 eV) were determined through a stepwise calibration procedure. First, the planar-averaged electrostatic potential along the direction perpendicular to the 2D plane (the z-axis) was computed, and the asymptotic plateau in the vacuum region was identified as the vacuum energy level (E_{vacuum}). It is noted that in VASP, the Fermi level (E_F) of an intrinsic semiconductor at 0 K is by default placed at the valence band maximum (VBM) rather than in the middle of the gap. Accordingly, the absolute VBM position was obtained by aligning the raw VBM eigenvalue against the vacuum reference as $E_{VBM} = E_{VBM,VASP} - E_{vacuum}$. The absolute conduction band minimum (CBM) was subsequently obtained by adding the HSE06 band gap directly to the calibrated VBM, *i.e.* $E_{CBM} = E_{VBM} + E_{gap,HSE}$. By anchoring the band edges directly to the VBM (which coincides with $E_{F,VASP}$ in our calculations) rather than assuming a mid-gap Fermi level, any rigid-shift artifacts in the absolute CBM and VBM positions relative to the vacuum reference are avoided.

Beyond satisfying the optimal band gap requirements, a viable photocatalyst must exhibit appropriate absolute band-edge alignments relative to the standard water redox potentials to successfully drive unassisted water splitting reactions. When evaluated on the absolute vacuum energy scale (E_{vacuum} = 0 eV), the standard reduction potential for hydrogen evolution (H^+/H_2) and the oxidation potential for oxygen evolution (O_2/H_2O) at pH = 0 are positioned at approximately $E_{red} = -4.44$ eV and $E_{ox} = -5.67$ eV, respectively.[61] Consequently, for a material to provide a sufficient thermodynamic driving force, its conduction band minimum (CBM) must be more positive (closer to the vacuum level, *i.e.*, $E_{CBM} > -4.44$ eV) than the reduction threshold, while its valence band maximum (VBM) must sit deeper on the energy scale (*i.e.*, $E_{VBM} < -5.67$ eV) than the oxidation threshold. As illustrated in Fig. 6, the absolute CBM and VBM levels are compared against these standard redox marks for the WSi_2N_4/AlSe, WSi_2N_4/GaSe, $WSiGeN_4$/AlSe, and $WSiGeN_4$/GaSe heterostructures under standard pH = 0 conditions. At this baseline level, the $WSiGeN_4$/AlSe heterostructure is the sole candidate that successfully straddles both limits simultaneously. However, because practical photocatalysis can be optimized by adjusting the chemical environment, evaluating these boundaries across a wider pH scope is highly desirable. The shifting behavior of the water redox potentials as a function of pH is governed by Nernstian relations obtained using eqn (3) and (4).[61] Fig. 7 provides a comprehensive representation of the pH-dependent VBM and CBM levels for these heterostructures. It has been demonstrated that the WSi_2N_4/AlSe heterostructure functions effectively within the pH range of 1 to 10, the WSi_2N_4/GaSe heterostructure within the pH range of 1 to 7, and the $WSiGeN_4$/AlSe heterostructure within the pH range of 0 to 5, as evidenced by the provision of VBM and CBM levels. However, the $WSiGeN_4$/GaSe heterostructure does not meet the band gap requirement and only meets the VBM level requirement. Consequently, this particular heterostructure will not be addressed in the ensuing discussions. Instead, the focus will be directed towards heterostructures that offer both band gap, CBM and VBM levels, where they are subjected to detailed examination.

$$E_{H^+/H_2} = (-4.44 + pH \times 0.059)\ eV \quad (3)$$

$$E_{O_2/H_2O} = (-5.67 + pH \times 0.059)\ eV \quad (4)$$

3.5 Charge density differences for the WSi_2N_4/XSe (X = Al and Ga) and $WSiGeN_4$/AlSe heterostructures

The charge separation and its transfer at the interface are crucial considerations for the heterostructures. These investigations are essential to determine the charge redistribution, electric field formation, *etc.*, for the photocatalyst heterostructures. The charge density differences are calculated using eqn (5) for the WSi_2N_4/XSe (X = Al and Ga) and $WSiGeN_4$/AlSe heterostructures. Fig. 8 shows the planar average charge density differences for these heterostructures, where positive (negative) values correspond to the electron accumulation (depletion) regions. The visualizations of the charge density differences are given as insets in the figures for top and side views. In these insets, cyan regions correspond to electron depletion while yellow ones correspond to electron accumulation. The following sequence, arranged in accordance with the charge density difference, is to be regarded as the most elevated to the least elevated: WSi_2N_4/AlSe, WSi_2N_4/GaSe, and $WSiGeN_4$/AlSe. Furthermore, the built-in electric field is shown as a black arrow directed from WSi_2N_4 and $WSiGeN_4$ to AlSe and GaSe monolayers. Another method of revealing the charge transfer is the Bader partial charge analysis, which has been shown to be a reliable and accurate technique. The WSi_2N_4/AlSe heterostructure has a charge transfer of $|0.015|e$ from the AlSe side to the WSi_2N_4 side, according to the calculated Bader partial charges. For the WSi_2N_4/GaSe heterostructure, the $|0.008|e$ charge is transferred from the GaSe side to the WSi_2N_4 side,

© 2026 The Author(s). Published by the Royal Society of Chemistry

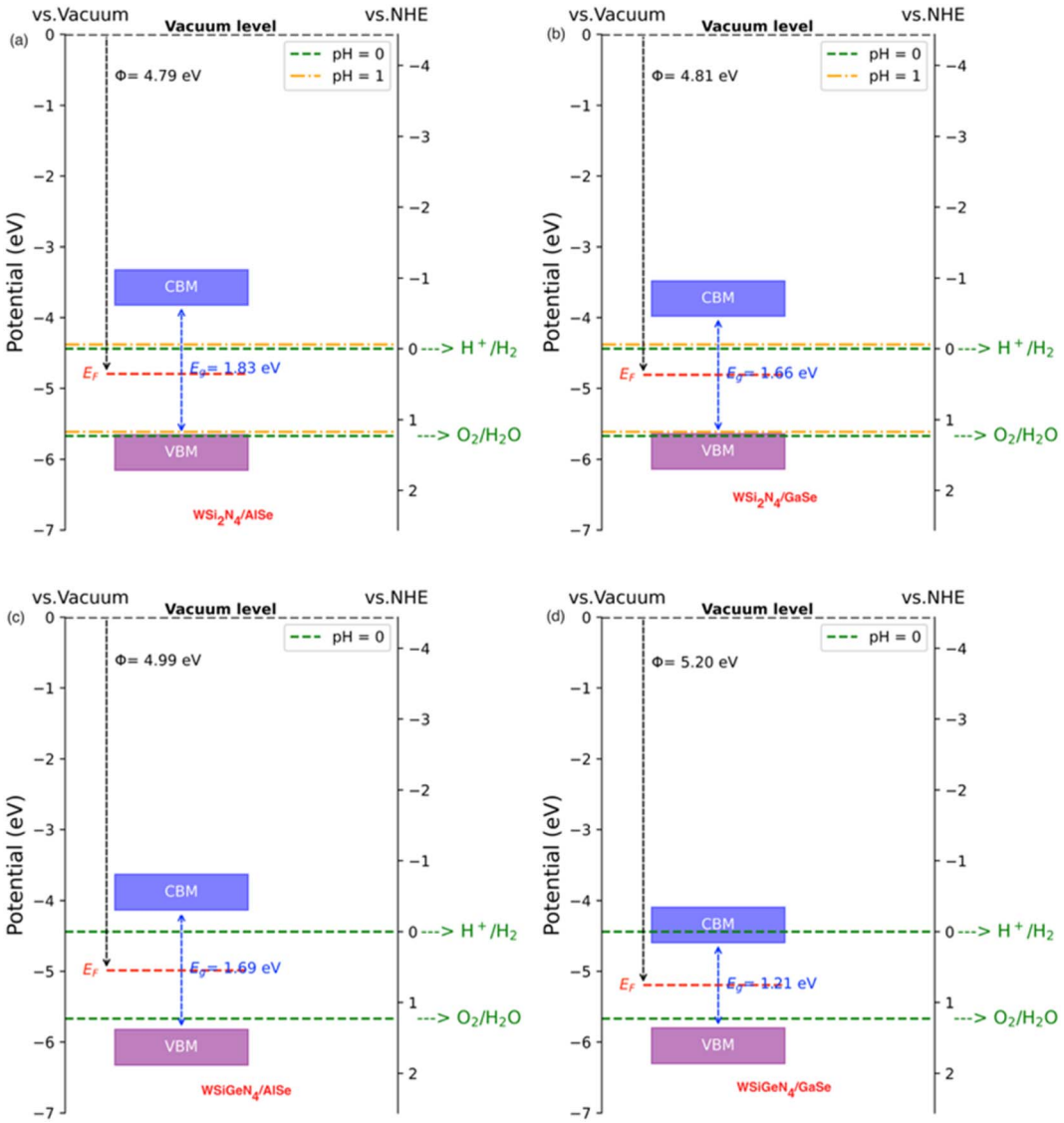


Fig. 6 CBM and VBM levels for (a) WSi_2N_4/AlSe, (b) WSi_2N_4/GaSe, (c) $WSiGeN_4$/AlSe, and (d) $WSiGeN_4$/GaSe heterostructures at pH = 0 condition.

whereas the $|0.014|e$ charge is transferred from the AlSe side to the $WSiGeN_4$ side, according to the calculated Bader partial charges. Although the integrated Bader transfers are modest in magnitude, as is typical for van der Waals interfaces with weak interlayer coupling, the directionality of the charge redistribution is unambiguous and fully consistent with the spatially resolved planar-averaged $\Delta\rho$ profiles shown in Fig. 8. The clear separation between electron-accumulation and electron-depletion regions along the interface, together with the consistent direction of the built-in electric field across the three heterostructures, provides robust evidence of an asymmetric interfacial dipole even though the net transferred charge per interface is small.

$$\Delta\rho = \rho_{WSi_2N_4/AlSe} - \rho_{WSi_2N_4} - \rho_{AlSe} \quad (5)$$

3.6 Mechanism for the photocatalytic water splitting for the WSi_2N_4/XSe (X = Al and Ga) and $WSiGeN_4$/AlSe heterostructures

In the domain of 2D heterostructure design for photocatalytic applications, a comprehensive understanding of the charge transfer mechanisms is imperative for enhancing the photocatalytic efficiency of these structures. The band alignment is of paramount importance for the carrier dynamics and redox potential. In a conventional type-II heterojunction, photogenerated electrons and holes migrate to different materials, resulting in spatial charge separation. However, this process often occurs at the expense of redox strength, as both charge carriers reside in lower-energy states. For an S-scheme mechanism, despite the similarities in band alignments between the two systems, the charge transfer behavior is distinct, fundamentally driven by differences in the individual monolayer work

© 2026 The Author(s). Published by the Royal Society of Chemistry

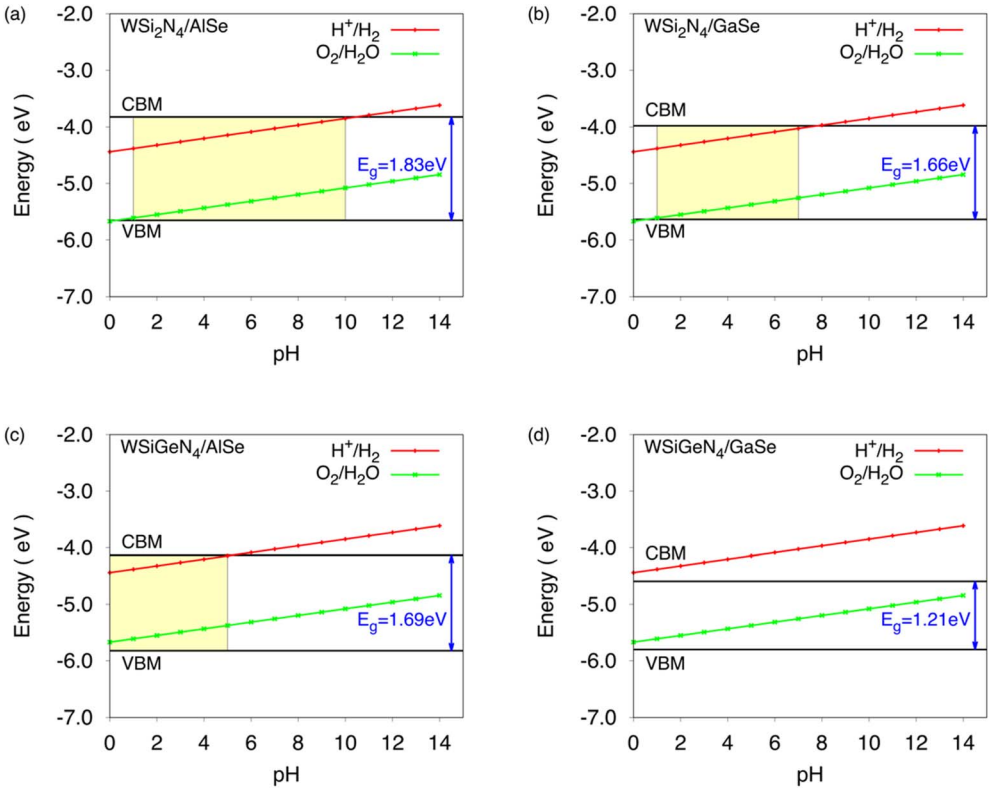


Fig. 7 pH-dependent CBM and VBM levels for (a) WSi_2N_4/AlSe, (b) WSi_2N_4/GaSe, (c) $WSiGeN_4$/AlSe, and (d) $WSiGeN_4$/GaSe heterostructures. The yellow rectangle shows the pH active region for the photocatalytic water splitting.

functions (Φ). Upon contact, electrons spontaneously flow from the material with the higher Fermi level (lower work function) to the one with the lower Fermi level (higher work function) until electrostatic equilibrium is achieved. This interfacial charge redistribution induces a built-in electric field (E_{bi}) and generates localized band bending at the contact region. Under light illumination, this E_{bi} and the resulting potential barrier act as a driving force: photogenerated electrons in the conduction band of the oxidation photocatalyst recombine with photogenerated holes in the valence band of the reduction photocatalyst at the interface. This selective recombination process has been shown to preserve the high-energy electrons in the conduction band of the reduction photocatalyst and the high-energy holes in the valence band of the oxidation photocatalyst, thereby maintaining the strong redox potential necessary for efficient photocatalytic reactions.

According to Fig. 9a and b, the WSi_2N_4/AlSe and WSi_2N_4/GaSe heterostructures exhibit this robust S-scheme mechanism. Due to the work function differences between the constituent monolayers, the contact induces a built-in electric field directed across the interface. Consequently, lower-energy photogenerated electrons in AlSe (or GaSe) recombine with lower-energy photogenerated holes in WSi_2N_4 at the interface. This selective recombination process preserves the high-energy, highly reducing electrons in the conduction band of WSi_2N_4 (with potentials well above the H^+/H_2 reduction potential) and the high-energy, highly oxidizing holes in the valence band of AlSe (or GaSe), maintaining the strong redox potential necessary for efficient photocatalytic reactions. The observed carrier dynamics, mediated by this equilibrium-induced interfacial band bending, confirm that these systems function *via* an S-scheme rather than a conventional type-II pathway. Conversely, as illustrated in Fig. 9c, the $WSiGeN_4$/AlSe heterostructure operates as a conventional type-II photocatalyst. In this configuration, the interfacial electronic environment facilitates the direct, unobstructed transfer of photogenerated electrons from the conduction band of $WSiGeN_4$ to the conduction band of AlSe and the concurrent migration of holes from the valence band of AlSe to the valence band of $WSiGeN_4$. This classic spatial separation suppresses recombination entirely, allowing the reduction and oxidation reactions to take place on separate layers, which is a hallmark of type-II behavior.

Beyond satisfying basic thermodynamic straddling constraints ($E_{CBM} > -4.44$ eV and $E_{VBM} < -5.67$ eV relative to the vacuum level), a highly efficient photocatalyst must provide an additional energy surplus, known as reaction overpotential, to overcome the kinetic barriers associated with surface reactions. As displayed in Fig. 9, the proposed S-scheme and Type-II heterostructures inherently meet these kinetic prerequisites. For instance, in the WSi_2N_4/AlSe (WSi_2N_4/GaSe) S-scheme mechanism (Fig. 9a/b), the active reduction electrons reside in the CBM of WSi_2N_4 (-2.85 eV), which translates to a massive driving potential of 1.59 eV above the H^+/H_2 level. Simultaneously, the oxidizing holes are retained in the VBM of AlSe/

© 2026 The Author(s). Published by the Royal Society of Chemistry

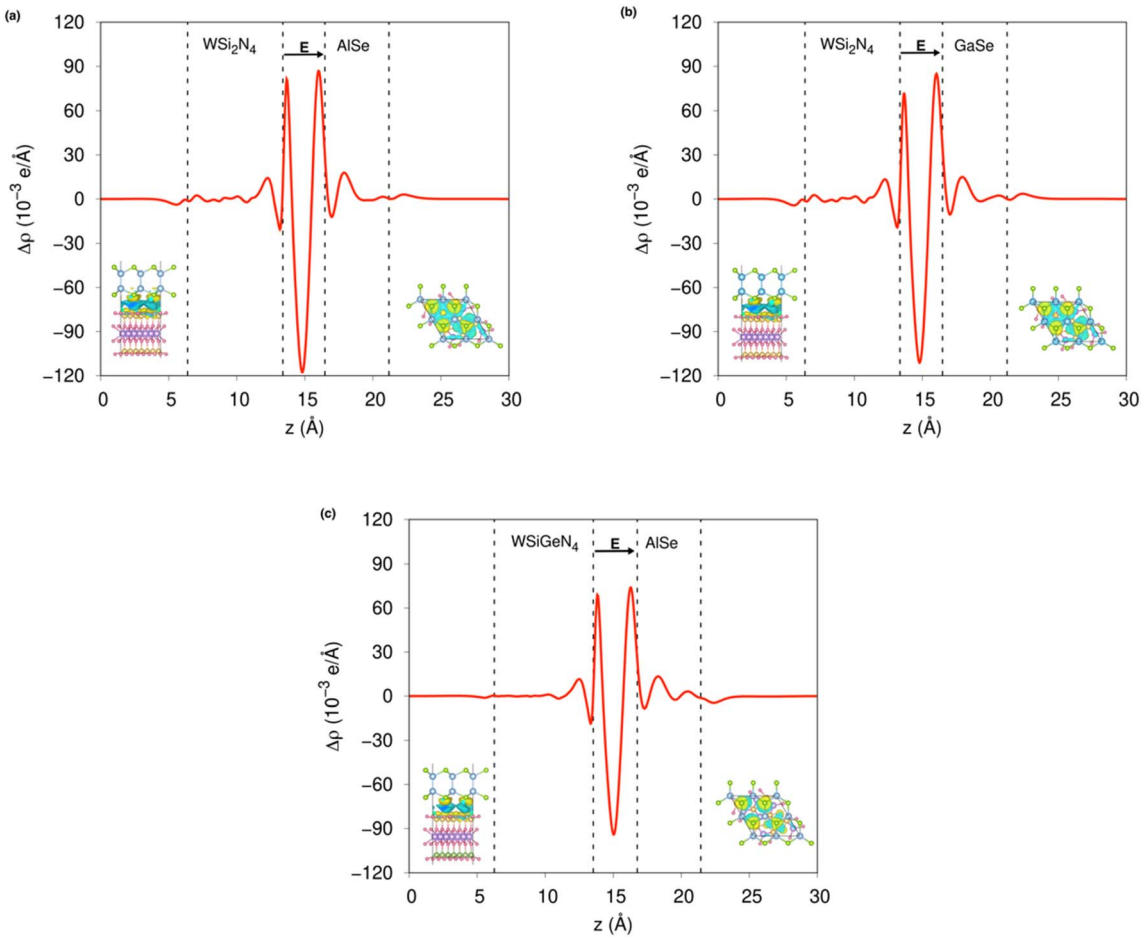


Fig. 8 Planar average charge density across the *z*-direction for (a) WSi_2N_4/AlSe, (b) WSi_2N_4/GaSe, and (c) $WSiGeN_4$/AlSe heterostructures. The insets show the visualizations of the charge density differences for top and side views. (Isosurface level is 0.0003 eÅ^{-3})

GaSe (−6.31/−6.32 eV), which provides a driving potential of 0.64/0.65 eV below the water oxidation level. For in the $WSiGeN_4$/AlSe type II mechanism (Fig. 9c), the active reduction electrons reside in the CBM of AlSe (−3.755 eV), which translates to a massive driving potential of 0.69 eV above the H^+/H_2 level. Simultaneously, the oxidizing holes are retained in the VBM of $WSiGeN_4$ (−5.76 eV), which provides a driving potential of 0.09 eV below the water oxidation level. These large energy margins vastly exceed the standard kinetic overpotential thresholds reported for 2D materials. Consequently, while explicit surface intermediate free-energy profiles remain an open avenue for future localized catalytic studies, our electronic structure analysis confirms that these heterostructures offer an exceptionally strong thermodynamic and kinetic driving force for complete, unassisted photocatalytic water splitting.

While the evaluated WSi_2N_4/AlSe, WSi_2N_4/GaSe, and $WSiGeN_4$/AlSe heterostructures satisfy the fundamental thermodynamic criteria for unassisted water splitting, it is important to clarify that absolute photocatalytic performance is ultimately a product of both electronic transport and surface reaction kinetics. A complete depiction of catalytic activity requires an evaluation of the Gibbs free-energy updates (ΔG) across the individual elementary steps of the hydrogen evolution reaction (HER) and oxygen evolution reaction (OER), alongside the explicit tracking of intermediate species adsorption (such as H*, OH*, and OOH*). Such surface-specific reaction pathway calculations are beyond the scope of this work, which focuses primarily on structural stability, hybrid-functional electronic screening, and fundamental charge carrier separation dynamics. Nonetheless, the prospective capabilities of these candidates are strongly reinforced by the immense potential gradients established by their respective S-scheme and Type-II configurations. The active conduction band of WSi_2N_4 sits roughly 1.6 eV above the hydrogen reduction threshold, while the active valence bands of the XSe layers sit up to 0.8 eV below the water oxidation threshold. Because these energetic margins substantially exceed the standard kinetic overpotential barriers reported for 2D layered catalysts, these systems are confirmed to possess excellent thermodynamic driving forces. Consequently, while localized surface engineering and explicit intermediate free-energy profiles remain an essential future direction, our electronic and optical results firmly classify these stable heterostructures as highly viable, thermodynamically robust candidates for visible-light-driven photocatalytic water splitting.

© 2026 The Author(s). Published by the Royal Society of Chemistry

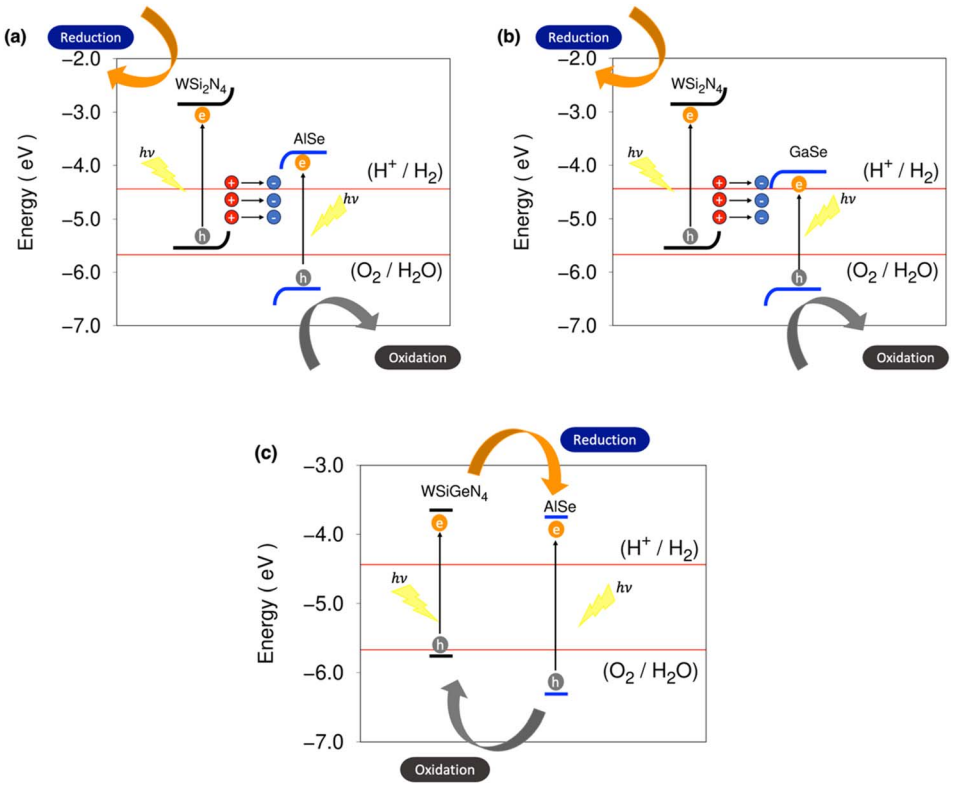


Fig. 9 Schematic diagrams of the photocatalytic mechanisms for (a) WSi_2N_4/AlSe, (b) WSi_2N_4/GaSe, and (c) $WSiGeN_4$/AlSe heterostructures.

To contextualize the performance and showcase the underlying novelty of the investigated configurations, a detailed comparison with previously reported MA_2Z_4-based heterostructures is organized in Table 4. Prior literature has explored systems like GaSe/WSi_2N_4,[26,27] WSi_2N_4/$MoSi_2N_4$,[27] and AlO/WSi_2N_4.[25,26] While a variation of a gallium selenide and tungsten silicon nitride pairing was examined in ref. 26, our specific structural orientation and layer configuration optimize the hybrid-functional electronic properties, dropping the direct band gap from 2.02 eV down to a highly visible-light-active 1.66 eV while successfully locking in the ideal S-scheme carrier dynamics. Furthermore, the introduction of the completely new WSi_2N_4/AlSe and Janus $WSiGeN_4$/AlSe systems expands the functional landscape of these materials. Notably, the transition from the pure WSi_2N_4 to the Janus $WSiGeN_4$ system triggers a fundamental change in the interface behavior, shifting the carrier path from an S-scheme to a Type-II mechanism. This clear comparative diversity underlines that the systems designed in this study offer superior, tailorable profiles for target-driven solar water splitting applications.

Table 4 Comparison of electronic properties, photocatalytic mechanisms, and operational pH ranges between the studied systems and previously reported MA_2Z_4-based heterostructures

Heterostructure	Band gap (eV)	pH-range	Mechanism	Reference
WSi_2N_4/AlSe	1.83 direct	1–10	S-scheme	This study
WSi_2N_4/GaSe	1.66 direct	1–7	S-scheme	This study
$WSiGeN_4$/AlSe	1.69 direct	0–5	Type-II	This study
GaSe/WSi_2N_4	2.02 direct	0–14	S-scheme	26
WSi_2N_4/$MoSi_2N_4$	2.007 direct	—	Type-II	27
AlO/WSi_2N_4	1.87 indirect	7	Type-II	25

3.7 Optical properties for the WSi_2N_4/XSe (X = Al and Ga) and $WSiGeN_4$/AlSe heterostructures

An exhaustive appraisal of their electronic characteristics has been expanded to encompass their optical properties for these heterostructures, to elucidate their potential for photocatalytic water splitting. The following procedure allows the frequency-dependent dielectric function to be evaluated. First, eqn (6) is to be applied, with the understanding that $\varepsilon_1(\omega)$ represents the real part and $\varepsilon_2(\omega)$ represents the imaginary part of the dielectric function.[63]

$$\varepsilon(\omega) = \varepsilon_1(\omega) + i\varepsilon_2(\omega) \quad (6)$$

As illustrated in Fig. 10(a), 11(a) and 12(a), the $\varepsilon_1(\omega)$ and $\varepsilon_2(\omega)$ are shown for the WSi_2N_4/AlSe, WSi_2N_4/GaSe, and $WSiGeN_4$/AlSe heterostructures, respectively, along the xx and yy directions. The $\varepsilon_1(\omega)$ has values of 5.00, 5.42, and 5.33 at 0 eV for the WSi_2N_4/AlSe, WSi_2N_4/GaSe, and $WSiGeN_4$/AlSe heterostructures, in that order. Furthermore, it has been established that the maximum value for $\varepsilon_1(\omega)$ is found in the visible region for these heterostructures. Examining the $\varepsilon_1(\omega)$ spectrum revealed no negative values, confirming that these monolayers are semiconductors within the 0–6 eV range.[64] The figure

© 2026 The Author(s). Published by the Royal Society of Chemistry

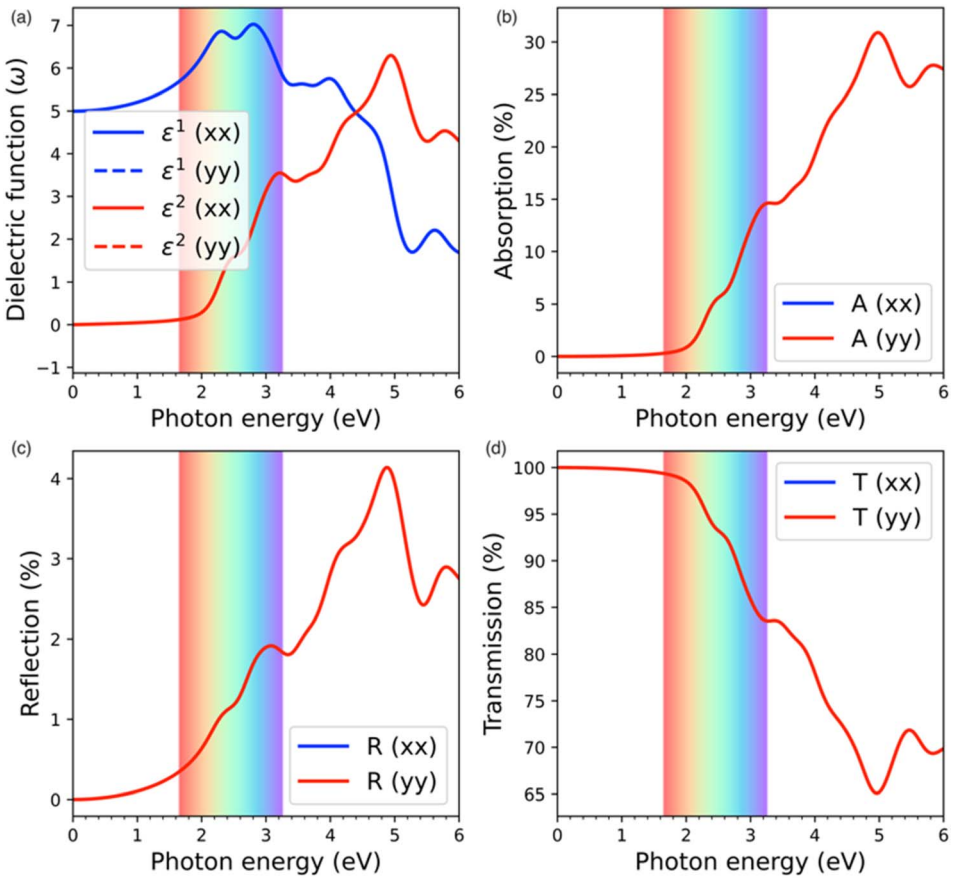


Fig. 10 (a) $\varepsilon_1(\omega)$ and $\varepsilon_2(\omega)$, (b) absorption, (c) reflection, and (d) transmission spectra of the WSi_2N_4/AlSe heterostructure (a rainbow bar shows the visible light region).

illustrates the parameter known as $\varepsilon_2(\omega)$, which is associated with the optical band gaps. The optical band gaps that have been calculated are 1.55 eV, 1.30 eV, and 1.26 eV for the WSi_2N_4/AlSe, WSi_2N_4/GaSe, and $WSiGeN_4$/AlSe heterostructures, respectively, and these align with the electronic band gaps that have been derived using the PBE method.

The absorption profiles along the xx and yy directions for the WSi_2N_4/AlSe, WSi_2N_4/GaSe, and $WSiGeN_4$/AlSe heterostructures are displayed in Fig. 10(b), 11(b), and 12(b), respectively where the visible light window (1.64 eV to 3.27 eV) is explicitly marked with a colored spectral gradient. To evaluate their solar energy harvesting efficiency, the absorption trends must be connected directly to photogenerated carrier production. All three candidate heterostructures display an ideal absorption onset (optical band gap threshold) in the range of 1.26–1.55 eV, lying just below or at the edge of the near-infrared-to-visible boundary. This low-energy onset ensures that the materials spontaneously initiate light absorption across the entire solar spectrum without wasting low-frequency visible photons. Here, the absorbance, reflectance, and transmittance percentages refer to the fraction of incident light absorbed, reflected, and transmitted by the two-dimensional monolayer heterostructure, computed from the frequency-dependent complex dielectric function and reported as dimensionless ratios in % to ensure intercomparability across the three candidate systems. A quantitative comparison within the visible spectrum reveals distinct performance traits among the candidates. The Janus $WSiGeN_4$/AlSe and the WSi_2N_4/GaSe heterostructures exhibit a steeper absorption climb, achieving an absorbance value of ~15% as the photon energy approaches 3.0 eV, which slightly exceeds the ~13% absorbance recorded for the WSi_2N_4/AlSe system. This robust visible-light utilization is further supported by the reflectivity profiles in Fig. 10(c)–12(c), which confirm that the surface reflectivity remains exceptionally low (<2%) throughout the visible region. Concurrently, the transmission spectra [Fig. 10(d)–12(d)] drop smoothly from ~100% down to ~83% across the same energy window. This inverse relationship proves that the attenuation of incident visible light is completely dominated by genuine electronic absorption rather than parasitic reflective scattering. As photon energies advance into the ultraviolet region (3.5 eV), all three systems exhibit a prominent absorption surge, peaking at over 30% between 4.5 eV and 5.0 eV. This broad-spectrum optical behavior—combining widespread visible light harvesting with intense ultraviolet capture—indicates that these heterostructures can maximize solar-to-hydrogen conversion pathways. By sustaining a continuous, highly efficient flux of photogenerated electrons and holes under natural sunlight, these optimized

© 2026 The Author(s). Published by the Royal Society of Chemistry

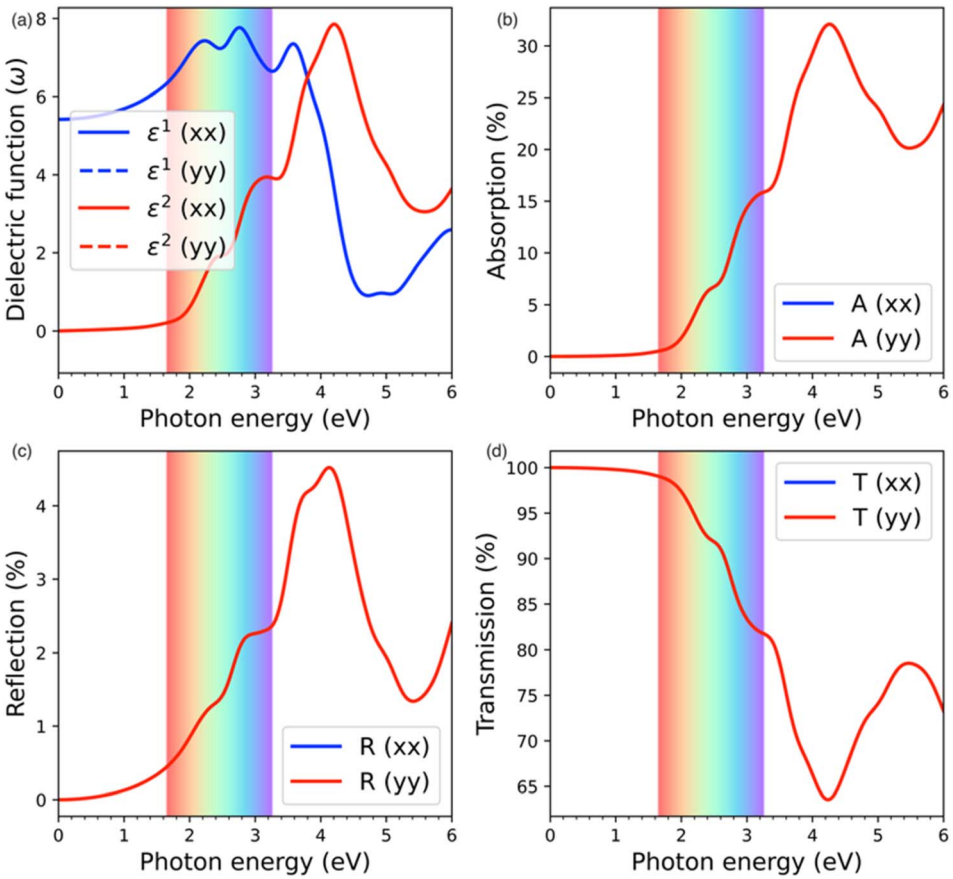


Fig. 11 (a) $\varepsilon_1(\omega)$ and $\varepsilon_2(\omega)$, (b) absorption, (c) reflection, and (d) transmission spectra of the WSi_2N_4/GaSe heterostructure (a rainbow bar shows the visible light region).

optical features provide an excellent foundation for driving continuous S-scheme and Type-II photocatalytic water splitting reactions.

3.8 Effect of water solvent for the WSi_2N_4/XSe (X = Al and Ga) and $WSiGeN_4$/AlSe heterostructures

Evaluating the integrity and electronic behavior of a photocatalyst within a fluid medium is of pivotal importance, as real-world solar water splitting occurs at a solid–liquid interface. To move beyond idealized vacuum approximations, the VASPSOL software package[48,49] was implemented to evaluate the heterostructures within an aqueous environment ($\varepsilon = 78.4$). The calculated solvation energies (E_{sol}) are summarized in Table 5. All values are consistently negative, spanning from −0.08 eV to −0.10 eV. Although the magnitudes are modest—on the order of a few times k_BT at room temperature—the consistently negative sign indicates that the immersion of the heterostructures in an aqueous dielectric medium is energetically favorable rather than destabilizing, suggesting that the layered structures retain their integrity against peeling or phase dissolution during catalytic operation.

The implicit solvent medium also introduces distinct changes to the electronic properties, as compiled in Table 5. Under aqueous conditions, the hybrid functional HSE06 band gaps undergo a subtle modification due to the dielectric modulation of electronic eigenvalues, yielding gaps of 1.73 eV, 1.56 eV, and 1.78 eV for WSi_2N_4/AlSe, WSi_2N_4/GaSe, and $WSiGeN_4$/AlSe, respectively. Crucially, all values remain safely above the fundamental 1.23 eV thermodynamic limit for water splitting. A meticulous evaluation of the absolute CBM and VBM levels under solvent conditions indicates that at pH = 0, the $WSiGeN_4$/AlSe heterostructure continues to act as the primary candidate satisfying the absolute straddling conditions ($E_{VBM} < -5.67$ eV and $E_{CBM} > -4.44$ eV). However, tracking the Nernstian shifts across varying pH levels (displayed in Fig. S9) shows that all three configurations exhibit highly adaptable, active operational windows under solvent conditions. Specifically, the valid band-straddling domain shifts to pH values of 5 to 11 for WSi_2N_4/AlSe, 4 to 9 for WSi_2N_4/GaSe, and 0 to 8 for $WSiGeN_4$/AlSe.

To visually isolate the solvent's role on interfacial dynamics, Fig. S11, S12, and S13 illustrate the comparative charge density differences ($\Delta\rho$) under both vacuum and aqueous environments. The spatial plots reveal a noticeable decrease in the magnitude of charge accumulation and depletion peaks upon immersion in water. This reduction is fundamentally driven by the dielectric screening effect of the high-permittivity aqueous medium ($\varepsilon = 78.4$). The polar solvent matrix reorganizes around

© 2026 The Author(s). Published by the Royal Society of Chemistry

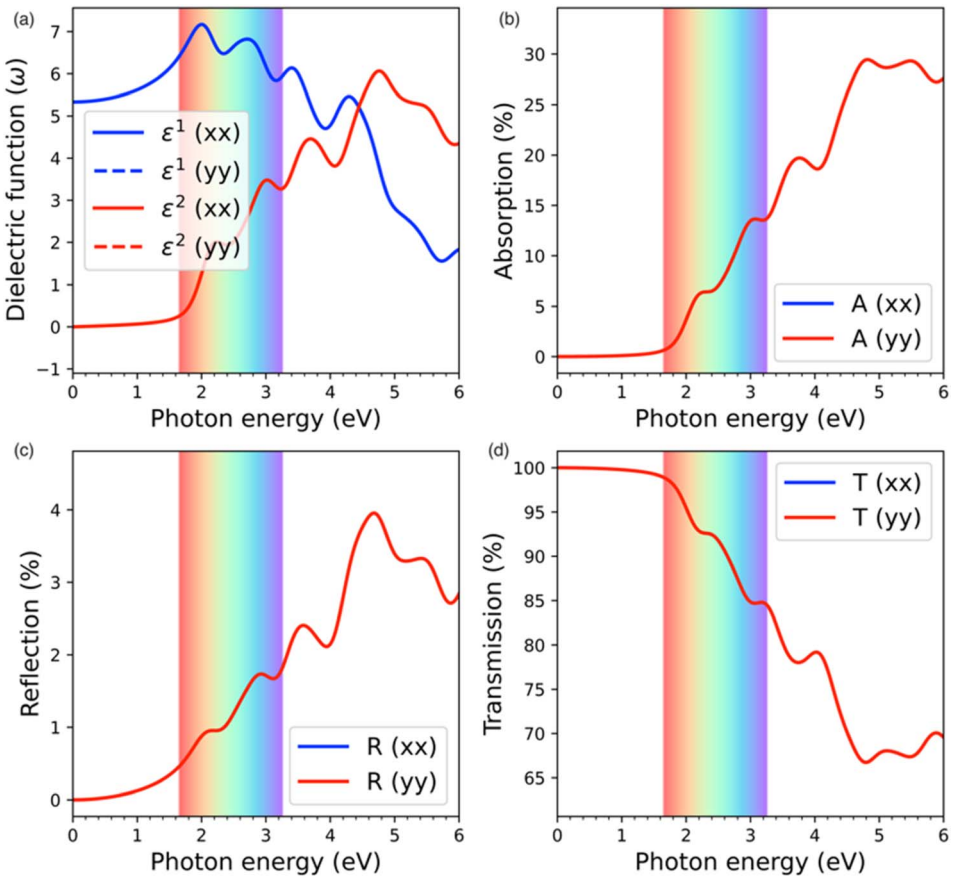


Fig. 12 (a) $\varepsilon_1(\omega)$ and $\varepsilon_2(\omega)$, (b) absorption, (c) reflection, and (d) transmission spectra of the $WSiGeN_4$/AlSe heterostructure (a rainbow bar shows the visible light region).

Table 5 Solvation energies (E_{sol}), HSE band gap (E_{gap}), VBM and CBM levels for WSi_2N_4/XSe (X = Al and Ga) and $WSiGeN_4$/AlSe heterostructures

	E_{sol} (eV)	E_{gap} (eV)	VBM (eV)	CBM (eV)
WSi_2N_4/AlSe	−0.08	1.73	−5.47	−3.74
WSi_2N_4/GaSe	−0.08	1.56	−5.45	−3.89
$WSiGeN_4$/AlSe	−0.10	1.78	−5.72	−3.93

the heterostructure to screen the internal dipole fields and built-in potential barriers. From a catalytic standpoint, this screening behavior is highly advantageous; by slightly softening the intense local charge clamping at the interface, the solvent reduces the activation energy for interplanar charge transport and suppresses localized carrier trapping. This allows the highly reactive, photogenerated carriers to easily migrate outwards from the bulk 2D matrix to the exposed surface, thereby maximizing the external quantum efficiency for fluid-phase hydrogen and oxygen evolution reactions.

While the negative E_{sol} values obtained *via* the VASPSOL implicit model confirm that the physical immersion of these heterostructures in an aqueous dielectric environment is thermodynamically favorable, it is imperative to distinguish physical solvation from chemical environmental stability. The implicit solvent model primarily accounts for macroscopic dielectric screening ($\varepsilon = 78.4$) and cannot predict the kinetic vulnerability of the exposed AlSe and GaSe layers to chemical degradation, such as hydrolysis or surface oxidation. As elegantly demonstrated in recent literature,[65] a rigorous evaluation of environmental stability requires explicitly mapping the molecular dissociation pathways and calculating the activation energy barriers (E_b) for H_2O and O_2 molecules on the material surfaces using methods such as Nudged Elastic Band (NEB).

Given the broad computational screening scope of the current study, explicitly modeling these chemical decomposition kinetics falls outside our present boundaries. Therefore, while our findings establish strong fundamental electronic and thermodynamic potential for the WSi_2N_4/AlSe and WSi_2N_4/GaSe heterostructures, their practical, long-term operational stability against water-induced chemical degradation remains an essential subject for future localized defect and reaction pathway investigations.

4. Conclusion

In the present study, a systematic first-principles investigation was conducted on the structural, electronic, and optical properties of WSi_2N_4/XSe and $WSiGeN_4$/XSe (X = Al, Ga, In) heterostructures, utilizing density functional theory to examine their

© 2026 The Author(s). Published by the Royal Society of Chemistry

thermodynamic potential for photocatalytic splitting of water. Initial screening configurations revealed that heterostructures formed with InSe possess positive binding energies, indicating their structural instability. For the remaining stable configurations, detailed electronic structure calculations utilizing PBE and HSE06 functionals demonstrated that while the $WSiGeN_4$/GaSe heterostructure exhibits an insufficient band gap (1.21 eV), the WSi_2N_4/AlSe, WSi_2N_4/GaSe, and $_{WSiGeN4}$/AlSe systems possess highly favorable, direct band gaps of 1.83 eV, 1.66 eV, and 1.69 eV, respectively. An examination of the VBM and CBM levels reveals that WSi_2N_4/AlSe is the sole material that satisfies the VBM and CBM condition at pH = 0. However, the effectiveness of a photocatalyst is contingent on its ability to operate over a broad pH range. Therefore, it is imperative to consider the pH range during which the material exhibits optimal performance. Specifically, WSi_2N_4/AlSe demonstrates efficacy within the 1–10 pH range, WSi_2N_4/GaSe exhibits optimal performance within the 1–7 pH range, and $WSiGeN_4$/AlSe displays its functionality within the 0–5 pH range, thereby satisfying the VBM and CBM conditions.

After the observation of these results, the charge transfer mechanisms of the above mentioned heterostructures were deduced. The WSi_2N_4/AlSe and WSi_2N_4/GaSe structures were found to have an S-scheme, while the $WSiGeN_4$/AlSe structure was found to have a type-II scheme. Consequently, the electron and hole pairs formed within these structures will undergo effective separation through these mechanisms. Furthermore, frequency-dependent optical spectra confirm stable visible-light utilization with minimal reflectivity losses, while implicit solvation models demonstrate that these systems retain favorable thermodynamic energy alignments when immersed in an aqueous environment.

In conclusion, this computational screening provides a thorough, theoretical evaluation of WSi_2N_4- and $WSiGeN_4$-based heterostructures. While definitive conclusions regarding operating catalytic efficiency remain subject to future surface kinetic calculations and experimental verification, our theoretical framework identifies these stable configurations as highly viable candidates for visible-light-driven solar water splitting. This work contributes a fundamental design blueprint to the ongoing development of low-dimensional materials for sustainable hydrogen production.

Author contributions

E. Turgut: writing – original draft, investigation, data curation. S. B. Lisesivdin: writing – review and editing, investigation, supervision, formal analysis. A. Gencer: writing – original draft, validation, methodology, conceptualization. O. Surucu: writing – original draft, investigation, conceptualization. G. Altuntas: writing – review and editing, investigation. B. Bostan: writing – review and editing, investigation. F. Himmet: writing – review and editing, investigation, data curation. G. Surucu: writing – review and editing, validation, supervision, methodology, conceptualization.

Conflicts of interest

There are no conflicts to declare.

Data availability

All data supporting the findings of this study, including the optimized crystal structures and complete atomic coordinate files (POSCAR), are available within the article's supplementary information (SI). Supplementary information is available. See DOI: https://doi.org/10.1039/d6ra03112a.

Acknowledgements

As outlined in this study, the numerical calculations were executed on the TRUBA resources available at TUBITAK ULAKBIM, High Performance and Grid Computing Centre, and at Istanbul Technical University National Center for High-Performance Computing. This latter institution is also known as ITU-UHEM, and the grant number for this project is 1024042025. This research was also facilitated by the Gazi University Scientific Research Projects Coordination Unit, which provided support under the project identification number FGA-2023-8982. Declaration of generative AI and AI-assisted technologies in the manuscript preparation process During the preparation of this work the authors used Google Gemini in order to enhance the language, clarity, and overall readability of the manuscript. After using this tool/service, the authors reviewed and edited the content as needed and take full responsibility for the content of the published article.

References

1 D. Gayen, R. Chatterjee and S. Roy, A review on environmental impacts of renewable energy for sustainable development, *Int. J. Environ. Sci. Technol.*, 2024, **21**, 5285–5310, DOI: 10.1007/S13762-023-05380-Z.

2 P. Meghna Gupta, Integrating Renewable Energy and Advanced Technologies for Sustainable Electricity Generation: A Comprehensive Review, *Proceedings - 2024 International Conference on Emerging Innovations and Advanced Computing*, INNOCOMP, 2024, pp. 695–702, DOI: 10.1109/INNOCOMP63224.2024.00120.

3 C. Gorea, D. L. Chiorean, I. Vlasa, I. Triștiu and D. Bica, Integration of Renewable Energy Sources in Energy Systems: Management, Security and Sustainability, *2023 11th International Conference on Enery and Environment*, CIEM, 2023, DOI: 10.1109/CIEM58573.2023.10349741.

4 J. Zhang and J. Li, Revolution in Renewables: Integration of Green Hydrogen for a Sustainable Future, *Energies*, 2024, **17**, 4148, DOI: 10.3390/EN17164148.

5 I. Dincer and M. I. Aydin, New paradigms in sustainable energy systems with hydrogen, *Energy Convers. Manage.*, 2023, **283**, 116950, DOI: 10.1016/J.ENCONMAN.2023.116950.

6 S. Nishioka, F. E. Osterloh, X. Wang, T. E. Mallouk and K. Maeda, Photocatalytic water splitting, *Nat. Rev. Methods Primers*, 2023, **3**(3), 1–15, DOI: 10.1038/s43586-023-00226-x.

© 2026 The Author(s). Published by the Royal Society of Chemistry

7 T. Hisatomi, Q. Wang, F. Zhang, S. Ardo, E. Reisner, H. Nishiyama, *et al.*, Photocatalytic water splitting for large-scale solar-to-chemical energy conversion and storage, *Front. Sci.*, 2024, **2**, 1411644, DOI: 10.3389/FSCI.2024.1411644.

8 F. Khodadadian, M. Nasalevich, F. Kapteijn, A. I. Stankiewicz, R. Lakerveld and J. Gascon, Photocatalysis: Past Achievements and Future Trends, RSC Green Chemistry, 2016pp. 227–269DOI: 10.1039/9781782623632-00227.

9 A. Singh and N. Sharma, Photocatalytic Hydrogen-Future Energy, *Mater. Chem. Phys.*, 2024, **322**, 129342, DOI: 10.1016/J.MATCHEMPHYS.2024.129342.

10 R. Sharma, M. Almáši, S. P. Nehra, V. S. Rao, P. Panchal, D. R. Paul, *et al.*, Photocatalytic hydrogen production using graphitic carbon nitride (GCN): A precise review, *Renew. Sustain. Energy Rev.*, 2022, **168**, 112776, DOI: 10.1016/J.RSER.2022.112776.

11 K. Ren, K. Wang, Y. Cheng, W. Tang and G. Zhang, Two-dimensional heterostructures for photocatalytic water splitting: a review of recent progress, *Nano Futures*, 2020, **4**, 032006, DOI: 10.1088/2399-1984/ABACAB.

12 C. Zhang, K. Ren, S. Wang, Y. Luo, W. Tang and M. Sun, Recent progress on two-dimensional van der Waals heterostructures for photocatalytic water splitting: a selective review, *J. Phys. D Appl. Phys.*, 2023, **56**, 483001, DOI: 10.1088/1361-6463/ACF506.

13 G. Wang, J. Chang, W. Tang, W. Xie and Y. S. Ang, 2D materials and heterostructures for photocatalytic water-splitting: a theoretical perspective, *J. Phys. D Appl. Phys.*, 2022, **55**, 293002, DOI: 10.1088/1361-6463/AC5771.

14 Y. L. Hong, Z. Liu, L. Wang, T. Zhou, W. Ma, C. Xu, *et al.*, Chemical vapor deposition of layered two-dimensional MoSi2N4 materials, *Science*, 2020, **369**, 670–674, DOI: 10.1126/SCIENCE.ABB7023/SUPPL_FILE/ABB7023_HONG_SM.

15 L. Wang, Y. Shi, M. Liu, A. Zhang, Y. L. Hong, R. Li, *et al.*, Intercalated architecture of MA2Z4 family layered van der Waals materials with emerging topological, magnetic and superconducting properties, *Nat. Commun.*, 2021, **12**(12), 1–10, DOI: 10.1038/s41467-021-22324-8.

16 Y. Yin, Q. Gong, M. Yi, W. Guo, Y. Yin, Q. Gong, *et al.*, Emerging Versatile Two-Dimensional MoSi2N4 Family, *Adv. Funct. Mater.*, 2023, **33**, 2214050, DOI: 10.1002/ADFM.202214050.

17 X. Wang, X. Li, X. Wang and W. Ju, Highly stable two-dimensional α1-MA2Z4 (M = Mg, Ca, Sr; A = Al; Z = S, Se) monolayers with promising photocatalysis and piezoresistive effect, *Appl. Phys. Lett.*, 2023, **123**(10), 103901, DOI: 10.1063/5.0168627.

18 C. Lin, X. Feng, D. Legut, X. Liu, Z. W. Seh and R. Zhang, Discovery of Efficient Visible-light Driven Oxygen Evolution Photocatalysts: Automated High-Throughput Computational Screening of MA2Z4, *Adv. Funct. Mater.*, 2022, **32**, 2207415, DOI: 10.1002/ADFM.202207415.

19 J. Chen and Q. Tang, The Versatile Electronic, Magnetic and Photo-Electro Catalytic Activity of a New 2D MA2Z4 Family, *Chem. Eur J.*, 2021, **27**, 9925–9933, DOI: 10.1002/CHEM.202100851.

20 M. Y. Liu, Y. He, X. Li and K. Xiong, Tuning of the electronic and photocatalytic properties of Janus WSiGeZ4 (Z = N, P, and As) monolayers via strain engineering, *Phys. Chem. Chem. Phys.*, 2023, **25**, 7278–7288, DOI: 10.1039/D2CP05224E.

21 Y. Yang, Y. Yu, Z. Liu, L. Shang, P. Xiang, Y. Xin, *et al.*, High-throughput computational screening of novel MA2Z4-type Janus structures with excellent photovoltaic and photocatalytic properties, *J. Mater. Chem. A*, 2024, **12**, 33233–33240, DOI: 10.1039/D4TA07195F.

22 F. Himmet, G. Surucu, S. B. Lisesivdin, O. Surucu, G. Altuntas, B. Bostan, *et al.*, Innovative 2D materials for efficient photocatalysis: A comparative study for WSi2N4, WGe2N4, and their janus counterpart WSiGeN4 monolayers, *Int. J. Hydrogen Energy*, 2024, **78**, 761–772, DOI: 10.1016/J.IJHYDENE.2024.06.304.

23 Z. Gao, X. He, W. Li, Y. He and K. Xiong, Janus XMoAZ2 (X = S, Se, Te; A = Si, Ge; Z = N, P, As) monolayers: First-principles insight into electronic structures, optical and photocatalytic properties, *Appl. Surf. Sci.*, 2023, **639**, 158146, DOI: 10.1016/J.APSUSC.2023.158146.

24 C. C. Tho, S. D. Guo, S. J. Liang, W. L. Ong, C. S. Lau and L. Cao, MA2Z4 family heterostructures: Promises and prospects, *Appl Phys Rev*, 2023, **10**, 041307, DOI: 10.1063/5.0156988.

25 C. Li, L. Xu, Z. Jin, Q. Wang, B. Xiao, Z. Li, *et al.*, Spontaneous enhanced photocatalytic overall water splitting on AlO/WSi2N4 vdW heterojunction, *Appl. Surf. Sci.*, 2024, **664**, 160247, DOI: 10.1016/J.APSUSC.2024.160247.

26 G. Yu, S. Huang, G. Qian, B. Lin and Q. Xie, S-scheme GaSe/WSi2N4 heterostructure with tunable bandgap for efficient photocatalytic hydrogen generation, *Mater. Today Commun.*, 2025, 113133, DOI: 10.1016/J.MTCOMM.2025.113133.

27 J. Bao, Y. Wang, X. Liu, R. Zhao, J. Yu and X. Chen, High-performance photocatalysts for overall water splitting: type-II WSi2N4/MoSi2N4 heterostructures, *New J. Chem.*, 2023, **47**, 16943–16953, DOI: 10.1039/D3NJ02761A.

28 G. Kresse and J. Furthmüller, Efficient iterative schemes for *ab initio* total-energy calculations using a plane-wave basis set, *Phys. Rev. B*, 1996, **54**, 11169, DOI: 10.1103/PhysRevB.54.11169.

29 G. Kresse and J. Furthmüller, Efficiency of ab-initio total energy calculations for metals and semiconductors using a plane-wave basis set, *Comput. Mater. Sci.*, 1996, **6**, 15–50, DOI: 10.1016/0927-0256(96)00008-0.

30 J. P. Perdew, K. Burke and M. Ernzerhof, Generalized Gradient Approximation Made Simple, *Phys. Rev. Lett.*, 1996, **77**, 3865, DOI: 10.1103/PhysRevLett.77.3865.

31 G. Kresse and D. Joubert, From ultrasoft pseudopotentials to the projector augmented-wave method, *Phys. Rev. B*, 1999, **59**, 1758, DOI: 10.1103/PhysRevB.59.1758.

32 P. E. Blöchl, Projector augmented-wave method, *Phys. Rev. B*, 1994, **50**, 17953, DOI: 10.1103/PhysRevB.50.17953.

© 2026 The Author(s). Published by the Royal Society of Chemistry

33 J. D. Pack and H. J. Monkhorst, "Special points for Brillouin-zone integrations"—a reply, *Phys. Rev. B*, 1977, **16**, 1748, DOI: 10.1103/PhysRevB.16.1748.

34 H. J. Monkhorst and J. D. Pack, Special points for Brillouin-zone integrations, *Phys. Rev. B*, 1976, **13**, 5188, DOI: 10.1103/PhysRevB.13.5188.

35 S. Grimme, J. Antony, S. Ehrlich and H. Krieg, A consistent and accurate ab initio parametrization of density functional dispersion correction (DFT-D) for the 94 elements H-Pu, *J. Chem. Phys.*, 2010, **132**, 154104, DOI: 10.1063/1.3382344.

36 Z. L. Liu, C. E. Ekuma, W. Q. Li, J. Q. Yang and X. J. Li, ElasTool: An automated toolkit for elastic constants calculation, *Comput. Phys. Commun.*, 2022, **270**, 108180, DOI: 10.1016/J.CPC.2021.108180.

37 S. M. Kastuar, C. E. Ekuma and Z. L. Liu, Efficient prediction of temperature-dependent elastic and mechanical properties of 2D materials, *Sci. Rep.*, 2022, **12**(12), 1–8, DOI: 10.1038/s41598-022-07819-8.

38 J. Heyd, G. E. Scuseria and M. Ernzerhof, Hybrid functionals based on a screened Coulomb potential, *J. Phys. Chem.*, 2003, **118**, 8207–8215, DOI: 10.1063/1.1564060.

39 A. V. Krukau, O. A. Vydrov, A. F. Izmaylov and G. E. Scuseria, Influence of the exchange screening parameter on the performance of screened hybrid functionals, *J. Chem. Phys.*, 2006, **125**, 224106, DOI: 10.1063/1.2404663.

40 A. M. Ganose, A. J. Jackson and D. O. Scanlon, sumo: Command-line tools for plotting and analysis of periodic ab initio calculations, *J. Open Source Softw.*, 2018, **3**, 717, DOI: 10.21105/JOSS.00717.

41 W. Tang, E. Sanville and G. Henkelman, A grid-based Bader analysis algorithm without lattice bias, *J. Phys.: Condens. Matter*, 2009, **21**, 084204, DOI: 10.1088/0953-8984/21/8/084204.

42 R. F. W. Bader, *Atoms in Molecules: A Quantum Theory*, Oxford University Press 1990, 438.

43 R. Jinnouchi, F. Karsai and G. Kresse, On-the-fly machine learning force field generation: Application to melting points, *Phys. Rev. B*, 2019, **100**, 014105, DOI: 10.1103/PhysRevB.100.014105.

44 R. Jinnouchi, F. Karsai, C. Verdi, R. Asahi and G. Kresse, Descriptors representing two-and three-body atomic distributions and their effects on the accuracy of machine-learned inter-atomic potentials, *J. Chem. Phys.*, 2020, **152**, 234102, DOI: 10.1063/5.0009491.

45 J. Behler and M. Parrinello, Generalized neural-network representation of high-dimensional potential-energy surfaces, *Phys. Rev. Lett.*, 2007, **98**, 146401, DOI: 10.1103/PhysRevLett.98.146401.

46 C. M. Bishop, *Pattern Recognition and Machine Learning, 2006*, Springer. Springer, 2016.

47 K. Momma and F. Izumi, VESTA 3 for three-dimensional visualization of crystal, volumetric and morphology data, *J. Appl. Crystallogr.*, 2011, **44**, 1272–1276, DOI: 10.1107/S0021889811038970/, https://journals.iucr.org/services/rss.html.

48 K. Mathew, R. Sundararaman, K. Letchworth-Weaver, T. A. Arias and R. G. Hennig, Implicit solvation model for density-functional study of nanocrystal surfaces and reaction pathways, *J. Chem. Phys.*, 2014, **140**, 084106, DOI: 10.1063/1.4865107.

49 K. Mathew, V. S. C. Kolluru, S. Mula, S. N. Steinmann and R. G. Hennig, Implicit self-consistent electrolyte model in plane-wave density-functional theory, *J. Chem. Phys.*, 2019, **151**, 234101, DOI: 10.1063/1.5132354.

50 F. Himmet, G. Surucu, S. B. Lisesivdin, O. Surucu, G. Altuntas, B. Bostan, *et al.*, Innovative 2D materials for efficient photocatalysis: A comparative study for WSi2N4, WGe2N4, and their janus counterpart WSiGeN4 monolayers, *Int. J. Hydrogen Energy*, 2024, **78**, 761–772, DOI: 10.1016/J.IJHYDENE.2024.06.304.

51 C. Das, M. Alam, D. Saikia, A. Betal, A. N. Gandi and S. Sahu, A Strategic Comparison Between Monolayers of WX2N4(X≒Si, Ge) Toward Thermoelectric Performance and Optoelectronic Properties, *Adv. Theory Simul.*, 2024, **7**, 2300981, DOI: 10.1002/ADTS.202300981.

52 M. Y. Liu, Y. He, X. Li and K. Xiong, Tuning of the electronic and photocatalytic properties of Janus WSiGeZ4 (Z = N, P, and As) monolayers via strain engineering, *Phys. Chem. Chem. Phys.*, 2023, **25**, 7278–7288, DOI: 10.1039/D2CP05224E.

53 Z. Haman, N. Khossossi, M. Kibbou, I. Bouziani, D. Singh, I. Essaoudi, *et al.*, Computational identification of efficient 2D Aluminium chalcogenides monolayers for optoelectronics and photocatalysts applications, *Appl. Surf. Sci.*, 2021, **556**, 149561, DOI: 10.1016/J.APSUSC.2021.149561.

54 K. Lazaar, M. Barhoumi and M. Said, A DFT study of GaSe/AlN(ZnO) two-dimensional vdW heterostructure practiced as an encouraging photocatalyst for water splitting, *Comput. Mater. Sci.*, 2022, **201**, 110912, DOI: 10.1016/J.COMMATSCI.2021.110912.

55 A. Bafekry, S. Karbasizadeh, M. Faraji, H. R. Jappor, A. A. Ziabari, M. M. Fadlallah, *et al.*, Electronic Performance and Schottky Contact of 2D GeH/InSe and GeH/In2Se3 Heterostructures: Strain Engineering and Electric Field Tunability, *Adv. Theory Simul.*, 2024, **7**, 2400438, DOI: 10.1002/ADTS.202400438.

56 F. Opoku, S. O. B. Oppong, A. Aniagyei, O. Akoto and A. A. Adimado, Boosting the photocatalytic H2 evolution activity of type-II g-GaN/Sc2CO2 van der Waals heterostructure using applied biaxial strain and external electric field, *RSC Adv.*, 2022, **12**, 7391–7402, DOI: 10.1039/D2RA00419D.

57 J. Chen, X. Wei, R. Zhang, J. Liu, Y. Tian, Y. Zhang, *et al.*, Type-II C2N/ZnTe Van Der Waals Heterostructure: A Promising Photocatalyst for Water Splitting, *Adv. Mater. Interfaces*, 2021, **8**, 2002068, DOI: 10.1002/ADMI.202002068.

58 H. Guo, B. Zhu, F. Zhang, H. Li, K. Zheng, J. Qiu, *et al.*, Type-II AsP/Sc2CO2 van der Waals heterostructure: an excellent photocatalyst for overall water splitting, *Int. J. Hydrogen Energy*, 2021, **46**, 32882–32892, DOI: 10.1016/J.IJHYDENE.2021.07.125.

© 2026 The Author(s). Published by the Royal Society of Chemistry

59 V. Wang, G. Tang, Y. C. Liu, R. T. Wang, H. Mizuseki and Y. Kawazoe, High-Throughput Computational Screening of Two-Dimensional Semiconductors, *J. Phys. Chem. Lett.*, 2022, **13**, 11581–11594, DOI: 10.1021/ACS.JPCLETT.2C02972.

60 M. Born and K. Huang, *Dynamical Theory of Crystal Lattices*, Oxford University Press, 1954.

61 L. Luan, L. Han, D. Zhang, K. Bai, K. Sun, C. Xu, *et al.*, AlSb/ZrS2 heterojunction: A direct Z-scheme photocatalyst with high solar to hydrogen conversion efficiency and catalytic activity across entire PH range, *Int. J. Hydrogen Energy*, 2024, **51**, 1242–1255, DOI: 10.1016/J.IJHYDENE.2023.09.156.

62 J. Li, Y. Yao, Y. Liu, Z. Gong, Z. Tang and X. Wei, A direct Z-scheme CuBiP2Se6/g-C3N4 heterojunction enhances the photocatalytic water splitting for hydrogen production: A DFT study, *Chem. Phys. Lett.*, 2025, **869**, 142056, DOI: 10.1016/J.CPLETT.2025.142056.

63 D. Mehta, Y. Naik, N. Modi, P. R. Parmar and P. B. Thakor, A theoretical investigation on optoelectronic and photocatalytic behaviour of Janus X-Ga-Al-Y (X, YS and Te) monolayers, *Solid State Commun.*, 2023, **375**, 115347, DOI: 10.1016/J.SSC.2023.115347.

64 S. Barma, M. S. Hasan Khan, M. R. Islam and M. T. Hasan, Intralayer spatial carrier separation capability for visible light driven photocatalytic properties of SnGe2N4-layered nanostructure: A first-principles study, *AIP Adv.*, 2023, **13**, 75020, DOI: 10.1063/5.0160594.

65 J.-A. Liu, L. Yin and G. Liu, Ferro/Nonferroelectric Vertical Heterostructure Superlattice as a Visible-Light-Responsive Photocatalyst: A DFT Prediction, *ACS Appl. Mater. Interfaces*, 2024, **16**(6), 7026–7037, DOI: 10.1021/acsami.3c15068.

© 2026 The Author(s). Published by the Royal Society of Chemistry